SPATIALLY-FILTERED CONTINUOUS-WAVE ACOUSTIC TOMOGRAPHY FOR BREAST CANCER DETECTION

by

Kevin McCaugherty
Bachelor of Engineering, University of Victoria 2010

A thesis submitted in partial fulfillment of the requirements for the Degree of

MASTER OF APPLIED SCIENCE

in the Department of Mechanical Engineering

Supervisory Information

Spatially-Filtered Continuous-Wave Acoustic
Tomography for Breast Cancer Detection

by

Kevin McCaugherty
B. Eng., University of Victoria, 2010

Supervisory Committee

Dr. Rodney Herring, Department of Mechanical Engineering
Supervisor

Dr. Barbara Sawicki, Department of Mechanical Engineering
Departmental Member

Dr. Adam Zielinski, Department of Electrical and Computer Engineering
Outside Member

Supervisory Committee

Dr. Rodney Herring, Department of Mechanical Engineering
Supervisor

Dr. Barbara Sawicki, Department of Mechanical Engineering
Departmental Member

Dr. Adam Zielinski, Department of Electrical and Computer Engineering
Outside Member

Abstract

The main objective of this master's thesis is to investigate the possibility of applying spatially-filtered continuous-wave acoustic tomography to the detection of breast cancer. A continuous acoustic wave is transmitted through the specimen in this tomographic imaging method. Any scattered waves that do not positively contribute to the projection are filtered out using an aperture. There is evidence to suggest that cancerous lesions in the breast have a higher speed of sound than surrounding tissues. This imaging method produces two tomograms of the specimen simultaneously: one showing the internal speed of sound, and the other showing the internal acoustic attenuation coefficient. There is the possibility for a third imaging modality, acoustic dispersion tomography, to be applied to this imaging method.

Two proof-of-concept prototype spatially-filtered continuous-wave acoustic tomography scanners were designed and built: one that uses a collimated beam to interrogate the specimen, and another that uses a confocal beam. A least-squares tomographic reconstruction algorithm was chosen to reconstruct the tomograms this method creates. A prostate phantom and a breast phantom were imaged with the confocal tomographic scanner. The tomograms of the prostate phantom show two 1 cm lesions which are consistent with information from the phantom manufacturer. Further work is required to properly validate the speed of sound and acoustic attenuation measurements this method produces.

Table of Contents

List of Tables

Table of Figures

Abbreviations and Terminology

ill-posed problem – a problem that does not possess one or more of the following traits: a solution exists; the solution is unique; the solution is well behaved (a small change in input leads to a small change in output).

inconsistent system of equations – a system of equations that has no solution because it is possible to derive a contradiction from the equations. Usually results due to the inclusions of errors in the data set.

overdetermined system – a system of linear equations whose equations outnumber the unknowns.

sensitivity – in a binary test, the proportion of actual positives correctly identified as such.

specificity – in a binary test, the proportion of actual negatives that are correctly identified as such.

symmetric matrix – a square matrix equal to its transpose.

symmetric positive-definite matrix – a symmetric matrix M is said to be positive definite iff $z^T Mz$ is positive for all non-zero column vectors z.

tomogram – a sectional image produced using tomography.

tomography – refers to imaging by sections or sectioning, typically with the use of a penetrating wave.

underdetermined system – a system of equations whose unknowns outnumber the equations.

List of Symbols

$\boldsymbol{\alpha}$	angle or angle vector (bold lowercase indicates a vector)
α	acoustic attenuation coefficient (absorption and scattering losses) [dB/m]
α_R	reflection coefficient
α_T	transmission coefficient
c	speed of sound [m/s]
$\boldsymbol{d}$	discrete data set
$\in$	element of
f	frequency [Hz]
$\boldsymbol{G}$	set of governing equations (i.e. ray paths) or geometry matrix (bold uppercase indicates a matrix)
$\boldsymbol{G^T}$	the transpose of the matrix $\boldsymbol{G}$
$\boldsymbol{G^{-1}}$	the inverse of the matrix $\boldsymbol{G}$
I	acoustic intensity [W/m^2]
$\boldsymbol{I}$	identity matrix
k	wave number
λ	wavelength [m], relaxation parameter
$\widetilde{\boldsymbol{m}}$	an approximate solution to $\boldsymbol{m}$
p	pressure [N/m^2]
$\mathbb{R}^m$	an m dimensional space of real numbers
ρ	density [kg/m^3]
Z	acoustic impedance [kg/m^{2}s]

CHAPTER 1 – INTRODUCTION AND MOTIVATION

1.1 INTRODUCTION

For many centuries those practicing medicine have used the mechanical properties of tissues as a means for diagnosis. Palpation is the act of assessing a patient with the hands. In this way, the practitioner can check the firmness of tissues and locate hard, dense regions that are perhaps indicative of abnormalities. While this method of examination is by no means quantitative or systematic, it does leave us an intuitive sense that the density and elastic properties of diseased tissues are different from healthy ones.

Tomography was born of the need to see inside an object without physically cutting it open to inspect it visually. Electromagnetic waves in the visible spectrum penetrate no more than a few centimeters into living tissue, making them poor candidates for tomography. EM waves in the x-ray spectrum do readily penetrate living tissues; however, they do not provide high contrast in soft tissues and expose the patient to ionizing radiation. Ultrasound, with a frequency of between 1 and 10 MHz, readily penetrates soft tissue and remains coherent for tens of centimeters. Ultrasound has a high level of interaction with soft tissues, and is ideally applied to imaging them.

The speed of sound in an object is based on its density and its resistance to uniform compression. It is for this reason that the speed of sound (both longitudinal and transverse) has been used as a quantitative metric for the diagnosis of disease. One disease in particular, cancer, shows promise in this area. The abnormal tissue growth associated with cancer makes it ideal for detection

with ultrasound. It has been shown that breast cancers have different acoustic properties from their surrounds [1–6]. It is for this reason that acoustic tomography has been proposed as a new imaging method for diagnosing breast cancer.

This thesis presents a method of acoustic tomography that produces both speed of sound and acoustic attenuation images by interrogating the specimen with a continuous ultrasonic wave. The change in phase of this wave is used to determine the time of flight through the object, while scattered waves that do not positively contribute to the image are removed by spatial filtering.

The goal of this work was to obtain quantitative data on how well spatially-filtered continuous-wave acoustic tomography might perform as a method for medical imaging. This was done by constructing two prototype tomography scanners based on the same working principle. One design was then used to measure the speed of sound inside a prostate phantom, as well as record a projection image of a breast phantom. A novel imaging modality, dispersion tomography, is also described and recommended for future investigation.

1.2 MOTIVATION

X-Ray mammography is the most widely used method in screening for breast cancer. This is a mature technology; however, there is much room for improvement. X-Ray mammography has been shown to have a sensitivity of as low as 40%, and a specificity of 93%. MRI has a sensitivity of 77% in detecting breast cancer [7]; however, the wide-spread use of MRI as a screening tool is not cost effective.

Reflection based ultrasound is commonly used to guide needle biopsies of breast lesions. It has not found widespread use as a screening tool primarily

because it is susceptible to human error: it is easy for the sonographer to miss a region in the breast, or miss a suspicious area altogether [8].

A systematic imaging modality that relies on a quantitative metric to diagnose breast cancer would be of considerable benefit. Acoustic tomography promises to provide this capability to healthcare professionals. It is for this reason that further development and innovation in this field is of importance.

1.3 Structure of the Thesis

The goal of this thesis is to present spatially-filtered continuous-wave acoustic tomography, the background knowledge required for an understanding of the method, and the design and construction of two prototype scanners and the measurements obtained with them.

The chapters of this thesis are organized in the following way:

- *Chapter 2* provides background information on the use of acoustic tomography for breast cancer detection. A brief description of tomography and inverse problem theory is presented, including the tomographic methods considered for reconstructing images. The propagation of acoustic waves is also presented. Finally, methods for detecting breast cancer are discussed.
- *Chapter 3* describes spatially-filtered continuous-wave acoustic tomography and presents the work done previously by others which provided a foundation for this work.
- *Chapter 4* lists the components used to construct the "collimated" and "confocal" prototype scanners and describes the phantoms used in imaging.

- *Chapter 5* presents experimental measurements made by the "confocal" scanner. These include a two-dimensional projection of a breast phantom and a tomogram of a prostate phantom.
- *Chapter 6* provides a discussion of spatially-filtered continuous-wave acoustic tomography and some recommendations for future avenues of work and exploration.

CHAPTER 2 – BACKGROUND INFORMATION

2.1 TOMOGRAPHY AND INVERSE PROBLEMS

The *inverse* problem lies in reconstructing the parameters that characterize a system from the result of some physical measurements [9]. Inverse problems arise when hidden or internal system information needs to be solved for. In solving an inverse problem, measurements are used to determine the properties of a physical object or system that cannot be directly observed. The relationship between observed data and the physical system is dependent on some known governing equations. In general, discrete linear inverse problems take the form:

$$\boldsymbol{d} = \boldsymbol{G}\boldsymbol{m}, \tag{1}$$

where: $\boldsymbol{d} \in \mathbb{R}^m$ is the output (or recorded data),
$\boldsymbol{m} \in \mathbb{R}^n$ is the system to be solved for (the object, in vector form), and
$\boldsymbol{G} \in \mathbb{R}^{m \times n}$ is the set of governing equations, or geometry matrix which maps the data $\boldsymbol{d}$ to the object $\boldsymbol{m}$.

The objective is to find some system $\boldsymbol{m}$ that produces the output $\boldsymbol{d}$ given the forward operator $\boldsymbol{G}$, which is the set of governing equations that relate input and output. It is convenient to treat the object as a vector of unknowns instead of a matrix of points in space: this allows for easy manipulation of the problem. The matrix $\boldsymbol{G}$ is typically a discretization of an ill-posed problem, e.g. the discrete Radon transform. The system of equations in equation 1 is said to be overdetermined when $m > n$ and underdetermined when $m < n$.

2.1.1 TOMOGRAPHY

Tomography is a method for determining the internal features of an object through the creation of sections, or tomograms [10], that are mathematically calculated from measured data without physically cutting the object. Tomography commonly takes the following form: the object of interest is queried by an interrogating wave or beam – as the beam passes through the object the amplitude and phase of the beam are modified. This modification is then recorded, and arranged into projections – called as such because the recorded beam contains the sum of all interactions as it passed through the object, thus 'projecting' the three-dimensional specimen onto a two-dimensional imaging plane. Many projections are taken at different viewing angles, and from these a tomogram is constructed.

Tomography has been employed in radiology (medicine), archaeology, biology, geophysics, oceanography, and materials science to study specimens with a wide range of compositions using a wide range of wave lengths.

Johan Radon was the first to discover that a two-dimensional function could be reconstructed from projections. The Radon integral is presented below:

$$Rf(L) = \int_L f(\boldsymbol{x})|d\boldsymbol{x}| \qquad 2$$

where: $f(\boldsymbol{x})$ is a continuous function vanishing outside a large disc in $\mathbb{R}^2$, and $Rf(L)$ is a function defined on the space of all straight lines in $\mathbb{R}^2$ by the line integral along each line.

Radon formulated this theorem of reconstructing a two-dimensional function from line integrals (projections) in 1917. This theorem shows that it is mathematically possible to transform projections of an object back into a representation of that object. The first practical image reconstruction formulism

was developed in the 1970s with the invention of x-ray computed tomography. Typically, the Radon transform is expressed as:

$$Rf(\alpha, s) = \int_{-\infty}^{+\infty} f\big((t\sin\alpha + s\cos\alpha), (-t\cos\alpha + s\sin\alpha)\big)dt \qquad 3$$

where: $Rf(\alpha,s)$ is known as a sinogram,
with s being perpendicular to each projection α taken along the path t.

Figure 1 shows the forward and inverse Radon transforms of a Shepp-Logan head phantom. A discretized version of the sinogram $Rf(\alpha,s)$ is usually what is recorded during the imaging process in tomography. The function $f(x,y)$ can be perfectly reconstructed if all the line integrals of all projections are obtained without error: in reality this is never the case.

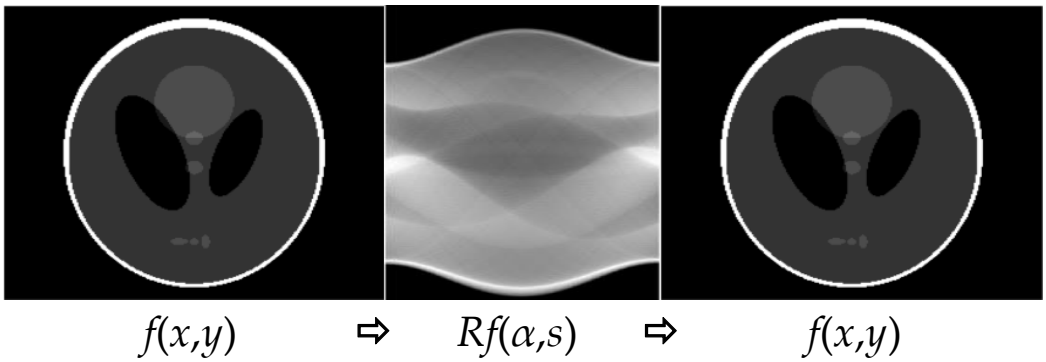

Figure 1: Forward and inverse Radon transforms of a Shepp-Logan head phantom.

An ill-posed problem is a problem that has no solution, or if a solution does exist the solution is not unique, or if the solution exists and is unique it is not well-behaved. In the strictest sense, tomographic reconstruction is an ill-posed overdetermined problem that has no solution. Reconstruction is ill-posed because all projections are not taken or are unavailable (an infinite number are required), there are errors in the projections (noise) which make the problem inconsistent, and because the recorded projections are quantized and discretized (detector-

pixels in each projection have a finite area and can only assume a finite number of values). Reconstruction is overdetermined because there are more recorded values in all the projections than unknown pixel values in the object space – necessary because the problem is ill-posed. One cannot simply apply Gaussian elimination to the system of equations obtained during imaging – there is no solution to the reconstruction problem, or if there is, this solution is a naïve solution and does not represent the object. The goal of reconstruction is to find an *approximate representation* of the object – not a direct solution to the reconstruction problem.

Any method that can provide an approximate solution to an ill-posed overdetermined system of linear equations can be used in tomographic reconstruction – several of them are briefly discussed in the next sections of this chapter.

2.1.2 Back Projection Methods

Back projection was one of the first techniques used in tomography. In essence, one simply takes the measured projections and simultaneously 'smears' them into the object space. This does not produce quantitatively accurate results, but does give a qualitative representation of the object.

Various schemes involving the convolution of projections with a modifying function produce much better quantitative results. To do this, the projections are transformed into a two-dimensional Fourier space and arranged around the origin according to what angle they were taken at. A filtering function is then convoluted with the transform: these functions aim to filter and weight different spatial frequencies in the data to reduce noise or increase edge prominence, and to correct the effect of the over- and under-sampling of regions within the object space. The

inverse two-dimensional Fourier transform is then applied, resulting in an image of the object.

Simple back projection is rarely used in practical applications, but filtered back projection is the most widely used method of image reconstruction in x-ray CT, including direct 3D reconstruction from 2D projection data.

2.1.3 LEAST-SQUARES

The method of least squares is an elegant approach to finding an approximate solution to an overdetermined system of equations. The solution is produced by minimizing the sum of the squares of the errors made in the result of every single equation. Least squares are popular for solving inverse problems because of their lack of complicated computations; however, least squares solutions have strong sensitivity to a small number of large errors (outliers) in the data set, and thus lack robustness [9]. This method is based on the assumption that errors in the data set are Gaussian. The linear least squares solution is:

$$\widetilde{\boldsymbol{m}} = (\boldsymbol{G}^T\boldsymbol{G})^{-1}\boldsymbol{G}^T\boldsymbol{d} \qquad 4$$

where: $\widetilde{\boldsymbol{m}}$ is an approximate solution to the system $\boldsymbol{m}$.

If the probability densities in the projections $\boldsymbol{d}$ are Gaussian, then the method of least squares approximates the solution to the error-free system very well (Carl Friedrich Gauss is credited with developing the fundamentals of the basis for least squares analysis).

For the solution of sparse data sets (such as those found in tomography), it is advantageous to add a relaxation parameter, λ. Typical values for λ range between 0.2 and 2. A modified least squares solution is computed as:

$$\tilde{\boldsymbol{m}} = (\boldsymbol{G}^T\boldsymbol{G} + \lambda\boldsymbol{I})^{-1}\boldsymbol{G}^T\boldsymbol{d} \quad (5)$$

where: $\boldsymbol{I}$ is the identity matrix.

2.1.4 Singular Value Decomposition

An important tool in analysing and solving inverse problems is Singular Value Decomposition (SVD). SVD is defined for any matrix $\boldsymbol{G} \in \mathbb{R}^{m\times n}$ as:

$$\boldsymbol{G} = \sum_{i=1}^{\min\{m,n\}} \boldsymbol{u_i}\boldsymbol{\sigma_i}\boldsymbol{v_i^T}, \quad (6)$$

where the vectors u_i and v_i are an orthonormal set (mutually orthogonal and of unit length), and$\boldsymbol{\sigma}$ is a matrix whose diagonal elements are $\sigma_1 \geq \sigma_2 \geq \ldots \geq \sigma_{\min\{m,n\}} \geq 0$, with all non-diagonal elements being zero. The elements σ_i are the singular values and the rank of matrix $\boldsymbol{G}$ is equal to the number of positive singular values. Assuming it exists, the inverse of $\boldsymbol{G}$ can be expressed as:

$$\boldsymbol{G^{-1}} = \sum_{i=1}^{\min\{m,n\}} \frac{1}{\sigma_i}\boldsymbol{v}_i\boldsymbol{u}_i^T \quad (7)$$

Using this expression for the inverse of $\boldsymbol{G}$, the naïve solution can be written as:

$$\boldsymbol{m} = \boldsymbol{G^{-1}d} = \sum_{i=1}^{\min\{m,n\}} \frac{\boldsymbol{u}_i^T\boldsymbol{d}}{\boldsymbol{\sigma}_i}\boldsymbol{v}_i \quad (8)$$

The naïve solution is called as such because of the susceptibility to any error in the input $\boldsymbol{d}$, which can lead to drastic changes in the output $\boldsymbol{m}$ (i.e., if the data set

contains any noise or other errors, the solution to that set of equations may be far distant from the actual, noise free solution).

SVD can be used to analyse inverse problems by observing the behaviour of the orthonormal vectors $\boldsymbol{u}$ and $\boldsymbol{v}$ and the singular values σ_i. The discrete Picard Condition [11] is satisfied when the coefficients $|\langle \boldsymbol{u}_i, \boldsymbol{d} \rangle|$ (absolute value of the inner product of $\boldsymbol{u}_i$ and $\boldsymbol{d}$) on average decay faster than the singular values σ_i [12]. Essentially, below this point (when $|\langle \boldsymbol{u}_i, \boldsymbol{d} \rangle|$ no longer decays faster than σ_i) the singular values do not add any more useful information to the solution, and are dominated by noise or uncertainty. If the discrete Picard condition is not satisfied for any values $|\langle \boldsymbol{u}_i, \boldsymbol{d} \rangle| < \sigma_i$, then the discrete ill-posed problem in question cannot be solved without further conditioning. For the purposes of this investigation, it is not necessary to understand why this is the case; however, it is useful to know that large errors in the naïve solution come from those values σ_i that lie below the Picard limit. With this in mind, the elimination or descaling of singular values below the Picard limit can lead to a better approximation to the solution. The truncated SVD method is defined as [12]:

$$\widehat{\boldsymbol{m}} = \sum_{i=1}^{k} \frac{\boldsymbol{u}_i^T \boldsymbol{d}}{\sigma_i} \boldsymbol{v}_i \qquad 9$$

where k has been chosen such that all the noise-dominated SVD coefficients are discarded.

2.1.5 Algebraic Reconstruction Techniques

Algebraic reconstruction techniques (ART) are a class of algorithms used in tomographic reconstruction, as well as in solving ill-posed linear inverse problems. ART methods are based on Kaczmarz's method, which involves the sequential

calculation of each equation G_i with a changing of the coefficients in $\boldsymbol{m}$ to try and match the data point d_i.

Various algorithms are used in this class of techniques. Presented here is Kaczmarz's method, which is the original and most commonly used algorithm in the ART class. The method is a row-action method, since each iteration consists of a sweep through all the rows in $\boldsymbol{G}$. As the method calculates one equation in each step, an iteration consists of m different steps (where m is the number of rows in the matrix $\boldsymbol{G}$). If the system is consistent (i.e., no noise), then Kaczmarz's method converges to a solution of the system. If it is inconsistent, every sub-sequence of iterations converges, but not necessarily to a least-squares solution. Kaczmarz's method converges very quickly in the first iterations which is why it has been adopted in tomography. Kaczmarz's Method is described below (for the solution to a problem of the form $\boldsymbol{Ax} = \boldsymbol{b},\ \boldsymbol{A} \in \mathbb{R}^{m\times n}$).

$$x^{k,0} = x^k,$$

$$x^{k,i} = x^{k,i-1} + \lambda_k \frac{b_i - \langle a_i, x^{k,i-1}\rangle}{\|a_i\|_2^2} a_i, \quad i = 1, 2, \dots, m, \qquad 10$$

$$x^{k+1} = x^{k,m}$$

where: k is the iteration number,
λ_k is an iteration-specific relaxation parameter,
$x^{k,i}$ is the current iteration vector in step i,
a_i is the row i of matrix A.

2.1.6 Simultaneous Iterative Reconstruction Techniques

The Simultaneous Iterative Reconstruction Techniques (SIRT) are a class of iterative methods where the information from all equations is used at once. They are designed to solve ill-posed linear inverse problems. All the algorithms in this

class can be written in the general form (for problems of the form $\boldsymbol{Ax} = \boldsymbol{b}$, $\boldsymbol{A} \in \mathbb{R}^{m \times n}$):

$$\boldsymbol{x}^{k+1} = \boldsymbol{x}^k + \lambda_k \boldsymbol{T}\boldsymbol{A}^T\boldsymbol{W}(\boldsymbol{b} - \boldsymbol{A}\boldsymbol{x}^k) \qquad k = 0, 1, \ldots \tag{11}$$

The different methods of this class depend on the selection of $\boldsymbol{W}$ and $\boldsymbol{T}$. Typically $\boldsymbol{T}$ is chosen as the identity matrix. One method in this class is the Landweber method [13], which can be written as follows:

$$\boldsymbol{x}^{k+1} = \boldsymbol{x}^k + \lambda_k \boldsymbol{A}^T(\boldsymbol{b} - \boldsymbol{A}\boldsymbol{x}^k), \quad k = 0, 1, \ldots \tag{12}$$

This corresponds to setting $\boldsymbol{W} = \boldsymbol{T} = \boldsymbol{I}$.

2.2 Acoustics

Acoustic imaging methods are applicable to substances transparent or semi-transparent to sound. They can be used to query optically opaque substances, and do not expose the specimen to ionizing radiation. Ultrasound (sound with a frequency above 22 kHz, the limit of human hearing) has been used in medical and non-destructive testing (NDT) for over 50 years. Low power exposure is generally considered safe for live specimens [14]. The United States Food and Drug Administration sets an intensity limit of 720 mW/cm^2 for ultrasound devices used for imaging humans. Frequencies in the low MHz range (1-10) are typically used to image living tissue, while frequencies of over 100 MHz can be used in NDT. Higher resolution can be obtained with a higher frequency, as described by the Rayleigh criterion:

$$\sin\theta = 1.220\frac{\lambda}{D} \tag{13}$$

where: θ is the angular resolution,
λ is the imaging wavelength,
and D is diameter of the imaging aperture.

In general, two methods of acoustic imaging exist: reflection-based methods, and transmission-based methods. In reflective methods, an acoustic pulse is transmitted into the specimen: the imaging system then 'listens' for the returning echo(s) from the specimen and records their intensity and time of arrival. This method is used in ultrasonic imaging and SONAR, among others. In ultrasonic imaging the intensity of the returning pulse is plotted against time, giving the appearance of two spatial dimensions, and forming a sectional image of the specimen. In transmission techniques, a pulse or continuous wave is transmitted through the specimen. The time of flight and the attenuation of the beam can be measured using this technique.

2.2.1 Speed of Sound in Fluids and Solids

The speed of sound is the rate at which a longitudinal wave travels through an elastic medium. The speed of an elastic wave in any medium is determined by the medium's compressibility and density – the speed of sound c in a homogeneous fluid is given as:

$$c_{fluid} = \sqrt{\frac{K}{\rho}} \qquad 14$$

where: c is the speed of sound,
K is the bulk modulus,
and ρ is the density of the fluid.

In solids, both longitudinal and shear waves can be sustained, as solids have a non-zero shear modulus. The speed of sound for shear and longitudinal waves can be different. For a homogeneous solid, the speed of longitudinal waves is given as:

$$c_{longitudinal} = \sqrt{\frac{K + \frac{4}{3}G}{\rho}} \qquad 15$$

where: K is the bulk modulus,
G is the shear modulus,

In a non-dispersive medium, the speed of sound is independent of the frequency of the wave. In a dispersive medium, the speed of sound is dependent on the frequency of the wave, and each frequency travels at its own phase velocity. Soft tissue has been shown to be slightly dispersive [15], while water is generally accepted as non-dispersive. Dispersion in sound speed is analogous to optical dispersion, but occurs for very different reasons.

In the continuous-wave spatially-filtered acoustic tomography imaging method water is used as a reference medium. Therefore, it is important to know the speed of sound in the tank housing the instrument. For this, Marczak's approximation for the speed of sound in pure water at atmospheric pressure as a function of temperature was used:

$$c_{water} = 1.402385 \text{ x } 10^3 + 5.038813 \text{ T} - 5.799136 \text{ x } 10\text{-}2 \text{ T}^2 + 3.287156 \text{ x } 10\text{-}4 \text{ T}^3 - 1.398845 \text{ x } 10\text{-}6 \text{ T}^4 + 2.787860 \text{ x } 10\text{-}9 \text{ T}^5 \qquad 16$$

where: c_{water} is the speed of sound in water, in [m/s]
T is the temperature in °C

This is an empirical relation derived from experimental results. Marczak's equation is considered accurate to within 0.02 m/s at temperatures between 0 and 95°C. Figure 2 shows the speed of sound in water versus the temperature.

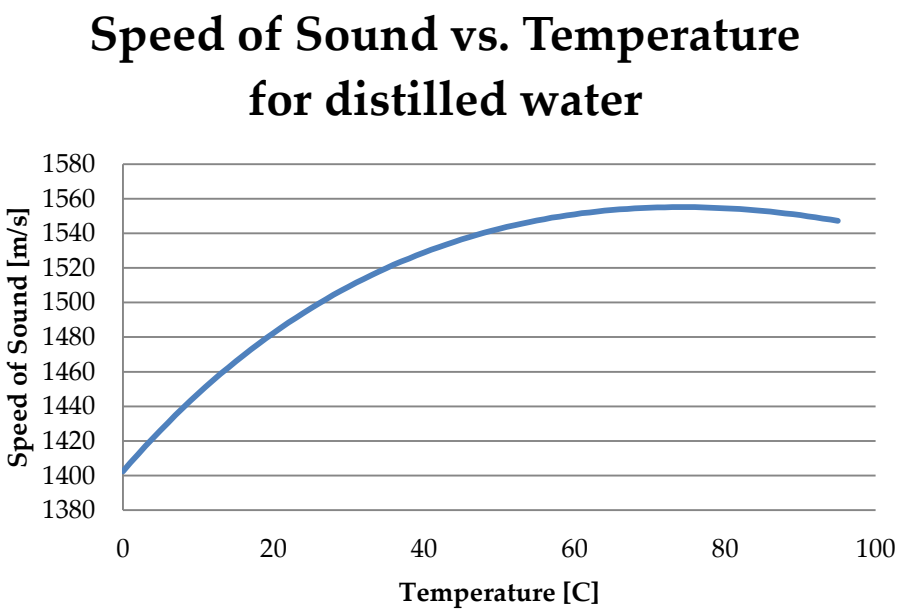

Figure 2: Speed of Sound in water as a function of temperature from Marczak's equation.

Typical temperature fluctuations in the lab (18 - 21°C) can produce up to a 10 m/s change in the speed of sound in water. Table 1 shows the speed of sound in some common liquids and solids at standard temperature and pressure.

Table 1: Speed of Sound in some common materials.

Material	Speed of Sound [m/s]
Ethanol	1144
Glycerine	1904
Aluminum	6420
Glass	3962
Zerdine™ [1]	1540 ± 40

[1] Zerdine is the proprietary tissue mimicking material used to create the prostate and breast phantoms.

2.2.2 ACOUSTIC INTENSITY

Acoustic intensity is the power per unit area carried by an acoustic wave. The intensity of an acoustic plane wave is defined as:

$$I(t) = \frac{p^2(t)}{\rho c} \qquad 17$$

where: I is the intensity [W/m^2],
p is the time varying pressure [Pa],
and ρ is the density of the medium [kg/m^3].

The value ρc is known as the acoustic impedance of a material, and is defined as:

$$Z = \rho c \qquad 18$$

where: Z is the acoustic impedance [kg/m^{2}s] or [Rayls].

Table 2 shows the acoustic impedance of some common materials.

Table 2: Acoustic impedances of some common materials.

Material	Acoustic Impedance [1E6 Rayls]
Ethanol	0.903
Glycerine	2.40
Aluminum	17.3
Glass	10.5
Zerdine™	1.59

The piezoelectric transducers used in both tomographic scanners will produce a voltage proportional to the pressure applied to the surface of the transducer. A harmonic acoustic plane wave travelling in a homogeneous fluid medium will produce a time varying pressure:

$$p(\boldsymbol{r},t) = |p|_1 \sin(\omega_0 t - \boldsymbol{k}\cdot\boldsymbol{r}) = |p|_1 e^{i(\omega_0 t - \boldsymbol{k}\cdot\boldsymbol{r})}, \qquad \omega_0 = 2\pi f \qquad 19$$

where: $|p|_1$ is the peak pressure of the wave (amplitude) [Pa],
f is the frequency of the wave [Hz],
$\boldsymbol{k}$ is the wavenumber, $2\pi/\lambda$ [m^{-1}]
λ is the wavelength [m]
and $\boldsymbol{r}$ is the distance of travel of the wave [m]

2.2.3 REFRACTION

Acoustic waves undergo a change in direction when they encounter a medium with a new speed of sound. Refraction occurs when a wavefront changes direction due to a change in the wave speed. The change in direction of light caused by lenses, the SOFAR channel[2], and mirages are all examples of refraction. The change in direction associated with passing between media with two different phase velocities is governed by Snell's law:

$$\frac{\sin(\theta_1)}{\sin(\theta_2)} = \frac{v_1}{v_2} \qquad 20$$

where: v_i is the phase velocity in medium i,
θ_1 is the angle of incidence of the ray, taken from normal,
and θ_2 is the angle of the refracted ray, taken from normal.

The phase velocity of a wave is the rate at which the phase of the wave travels in space. This is the velocity at which any one frequency will travel in the medium, and is frequency dependent in dispersive media.

Figure 3 shows the refraction of a sound ray for three different cases. When medium 1 has a smaller speed of sound than medium 2, the beam is refracted

[2] The SOFAR channel (Sound Frequency and Ranging channel) is a horizontal layer of water in the ocean where the sound speed is at its minimum (due to changing pressure, temperature and salinity). This layer acts as a waveguide, refracting sound waves back into the layer.

away from normal. When the two mediums have the same speed of sound, the wave is not refracted. When medium 1 has a larger speed of sound than medium 2, the beam is refracted towards normal.

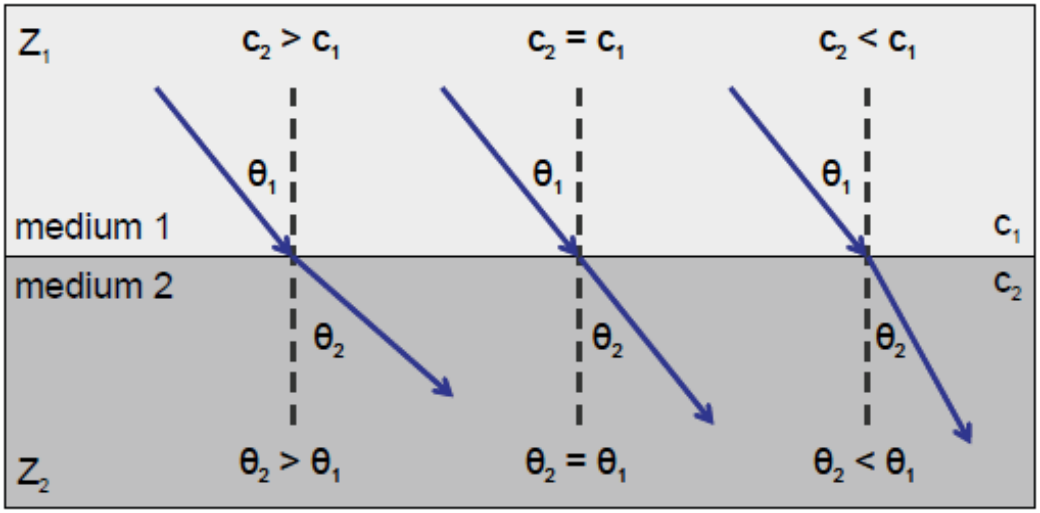

Figure 3: Snell's law of refraction for three different cases [16].

At some angle, known as the critical angle, the wave is completely reflected back into medium 1, and does not enter medium 2. This critical angle is found by setting θ_2 to 90°, and then solving for θ_1 using Snell's law. This gives rise to total reflection. It is also important to note that partial reflection can occur at angles less than the critical angle.

In general, acoustic waves travelling in moving inhomogeneous media can be described using the eikonal equation [17], [18]. If we describe the media by its spatially variant well-behaved speed of sound $c(\boldsymbol{r})$, and its velocity $\boldsymbol{v}(\boldsymbol{r})$, then the eikonal equation is given by:

$$\frac{c_0}{c(\boldsymbol{r})} - \frac{\boldsymbol{v}(\boldsymbol{r}) \cdot \nabla\xi(\boldsymbol{r})}{c(\boldsymbol{r})} = |\nabla\xi(\boldsymbol{r})| \qquad 21$$

where: c_0 is an arbitrary reference sound speed,

and ξ is the eikonal function (phase) of the wavefront.

It is important to note that this equation is non-linear. For the purposes of this text, we can ignore the velocity-field contribution. It is shown in [18] that the solution to the eikonal equation can be reduced to the integration of the differential equations:

$$\frac{d\boldsymbol{r}}{d\nu} = \frac{\boldsymbol{b}}{b}\,, \qquad \boldsymbol{b} = \nabla\xi\,, \qquad b = \frac{d\xi}{d\nu} \tag{22}$$

$$\frac{d\boldsymbol{b}}{d\nu} = -\frac{c_0 \nabla c}{c^2} \tag{23}$$

where: ν is the independent variable (nu),
and $\boldsymbol{r}(\nu)$ is the ray path of a sound wave in an inhomogeneous medium.

The ray path $\boldsymbol{r}(\nu)$ can be solved from (22) and (23). It is convenient to solve for the path in terms of the ray length s (or the distance along the path) or the time t. The relationship between t, s, and ν is given by:

$$\frac{d\boldsymbol{r}}{dt} = \boldsymbol{u}_g\,, \qquad d\nu = \frac{c\,ds}{u_g}\,, \qquad dt = \frac{ds}{u_g} \tag{24}$$

where: $\boldsymbol{u}_g$ is the velocity, and u_g is the amplitude of the velocity (speed).

2.2.4 Reflection and Transmission

When sound waves encounter a different medium, the acoustic intensity can be completely transmitted, partially transmitted and partially reflected, or completely reflected. As described by the Rayleigh model, the reflection coefficient, α_R, is given as:

$$\alpha_R = \frac{I_3}{I_1} = \left(\frac{K_2 - K_1}{K_2 + K_1}\right)^2 \tag{25}$$

where: I_1 is the incident acoustic intensity,
I_3 is the reflected acoustic intensity, and

$$K_1 = \frac{Z_1}{\cos(\theta_1)}, \qquad K_2 = \frac{Z_2}{\cos(\theta_2)}$$

Figure 4 shows a sound ray being partially reflected and refracted. The angle of reflection is equal to the angle of incidence, and the refracted ray follows Snell's law. The amount of reflected intensity depends on the angle of incidence, and the acoustic impedances of two media. The angles are all measured from normal, as with Snell's law.

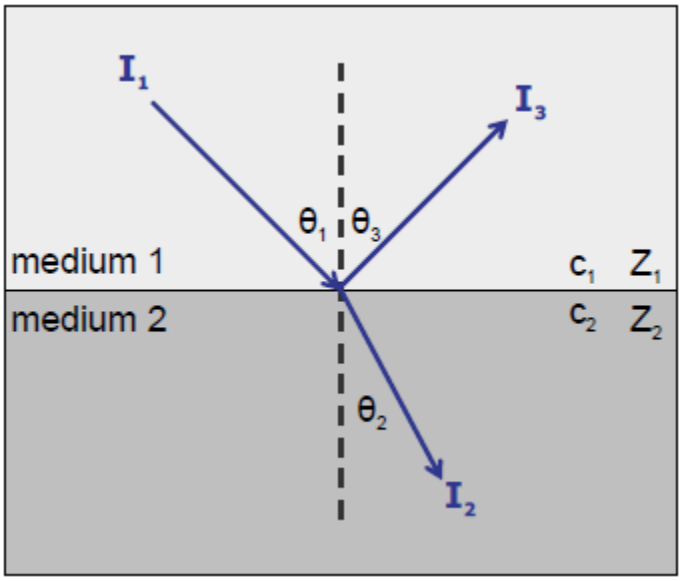

Figure 4: Sound reflection and refraction at an interface, showing partial transmission [16].

The transmission coefficient α_T also depends on these three factors. If we assume no absorption at the interface, then we have:

$$\alpha_R + \alpha_T = 1, \qquad \text{and} \qquad I_2 + I_3 = I_1 \tag{26}$$

From this, we can determine the transmission coefficient to be:

$$\alpha_T = \frac{I_2}{I_1} = \frac{4K_1K_2}{(K_1 + K_2)^2} \tag{27}$$

No phase shift in the reflected waves occurs when the angle of incidence is less than or equal to the critical angle. However, when the incident angle is greater than the critical angle a phase shift in the reflected wave occurs. The phase lag is given by:

$$\Delta\phi = -2\tan^{-1}\frac{b}{a}$$

$$a = Z_2\cos\theta_1\,,\quad b = Z_1\sqrt{\left(\frac{c_2}{c_1}\right)\sin^2\theta_1 - 1} \qquad 28$$

where: $\Delta\phi$ is the phase change.

From equations 25-28, we can determine that sound will be transmitted at any interface, except when $Z_1 >> Z_2$, $Z_1 << Z_2$, or $\theta_1 < \theta_{crit}$. When $\theta_1 < \theta_{crit}$, there is no phase shift in the reflected wave. When complete reflection occurs, there is a phase shift in the reflected wave. It is important to note that there is no phase shift in the transmitted wave due to a medium interface. Figure 15 in section 3.2.3 shows the reflection and transmissions coefficients for an aluminum / water interface from between 0 and 20 degrees.

2.2.5 Absorption

Sound energy absorbed by a medium is modeled as an exponential decay with distance, the rate of which is determined by the absorption coefficient $\alpha(f,\boldsymbol{r})$. This is written as:

$$I = I_0 \cdot 10^{-\frac{\alpha r}{10}} \qquad 29$$

where: I_0 is the acoustic intensity of the emitter [W/m^2],
I is the acoustic intensity at a location r, and
α is the absorption coefficient [dB/m].

The absorption coefficient generally depends on the frequency and the medium.

2.2.6 DIFFRACTION

Diffraction occurs when a wave encounters a partial path obstruction. This effect can be seen as a wavefront "bending" around the corners of a small object. It can also be seen as the spreading out of a wave past the exit of a small opening. Diffraction effects can generally be ignored when there are no large changes in the acoustic impedance inside a specimen, or when the wavelength is longer than twice the diameter of any small reflective inclusions.

2.3 BREAST CANCER DETECTION

Breast cancer is the most frequently diagnosed cancer, accounting for 22.9 % of all diagnosed cancers and 13.7% of all cancer related deaths in women [19]. X-ray mammography is the most widely used screening tool to detect early incidents of breast cancer [20].

2.3.1 X-RAY MAMMOGRAPHY

In 1913, it was discovered that x-rays could detect breast cancer in humans; however, it wasn't until the 1960's that the use of x-ray mammography (XRM) for screening and diagnosing breast cancer became widespread.

The method consists of the compression of the breast between two parallel plates: this is done to limit the overlapping of possible tumours and soft tissue features, and to allow for a reduction in the intensity of the x-ray source required for imaging. Two views of each breast are taken: mediolateral oblique (horizontal) and craniocaudal (vertical). In screening, the two views are reviewed independently by two radiologists to increase sensitivity. Additional views are taken at the direction of a radiologist during a diagnostic test. Not all women are

candidates for XRM because the density and / or complex arrangement of tissues in their breasts makes imaging unclear.

2.3.2 SCREENING

The use of XRM as a method for screening for breast cancer in otherwise healthy women is debated. One study has shown the sensitivity of a single XRM screening to be as low as 40% [7] with a specificity of 93%. The Cochrane report on the effectiveness of screening with XRM presented the following:

> Screening will… result in some women getting a cancer diagnosis even though their cancer would not have led to death or sickness. Currently, it is not possible to tell which women these are, and they are therefore likely to have breasts or lumps removed and to receive radiotherapy unnecessarily. The review estimated that screening leads to a reduction in breast cancer mortality of 15% and to 30% overdiagnosis and overtreatment. This means that for every 2000 women invited for screening throughout 10 years, one will have her life prolonged. In addition, 10 healthy women, who would not have been diagnosed if there had not been screening, will be diagnosed as breast cancer patients and will be treated unnecessarily. Furthermore, more than 200 women will experience important psychological distress for many months because of false positive findings. [21]

It is expected that a screening method featuring a high sensitivity and a high specificity would be beneficial, especially if it carried the same cost as XRM per visit.

2.3.3 Speed of Sound in the Human Breast

Li et al [6] found that the tissues that make up the breast have differing speeds of sound. Of particular interest was the finding that malignant breast lesions had a higher speed of sound (on average) than benign ones (however, the speed of sound distributions do overlap). Table 3 shows their findings.

Table 3: Speed of sound of various breast tissues [6].

Breast Tissue	Speed of Sound [mean ± SD]
fatty tissue	1422 ± 9 m/s
breast parenchyma[3]	1487 ± 21 m/s
malignant lesion	1548 ± 17 m/s
benign lesion	1513 ± 27 m/s

These results are promising for the use of the speed of sound as a diagnostic metric for breast cancer. However, they should be cautioned because of the small sample size (122 samples – 32 lesions), and the unknown accuracy of the test – further investigation is required. Greenleaf *et al.* [22] have also demonstrated that cancerous breast tissues have a different speed of sound than surrounding healthy tissues.

2.3.4 Acoustic Tomography for Breast Cancer Detection

A number of groups developed methods to measure the speed of sound and acoustic attenuation of the breast *in vivo* using acoustic tomography, including: Juřík *et al.* [23], Carson *et al.* [24], André *et al.* [4], Johnson *et al.* [25], and Duric *et al.* [1], [6]. In most methods, the object to be imaged is immersed in a tank of water and surrounded by a large number of transducers which insonify it. The transducers then record the transmitted and reflected / scattered waves created as a result of insonification.

[3] Parenchyma is the bulk of a substance. In this case, it refers to the functional parts of the mammary gland.

Duric *et al.* at the Karmanos Cancer Institute in Michigan have developed a prototype imager (dubbed CURE) capable of: 4 mm resolution in transmission imaging; the detection of masses greater than 15 mm in size; and reflection, speed of sound, and attenuation imaging modes. A ring-array of 256 piezoelectric transducers is used in a pulse-receive technique. The ring is then moved through different z-planes (up to 75) to create three-dimensional images. Tomograms are reconstructed using a bent-ray algorithm with total-variation regularization, and reflection images are obtained using a pulse-echo technique. The image acquisition time is approximately 1 minute. This system is currently undergoing clinical trials. Figure 5 shows the CURE system developed at Karmanos.

Figure 5: Karmanos CURE system showing the tank (a), and the transducer ring (b) [1].

The resolution of the CURE system is limited by the number of transducers used, as no rotation is employed to increase the number of viewing angles. However, because three imaging modes are used, they can be combined into one image without any geometric discrepancies.

Figure 6 shows a reflection, sound-speed, and attenuation image of a breast with an infiltrating ductal carcinoma.

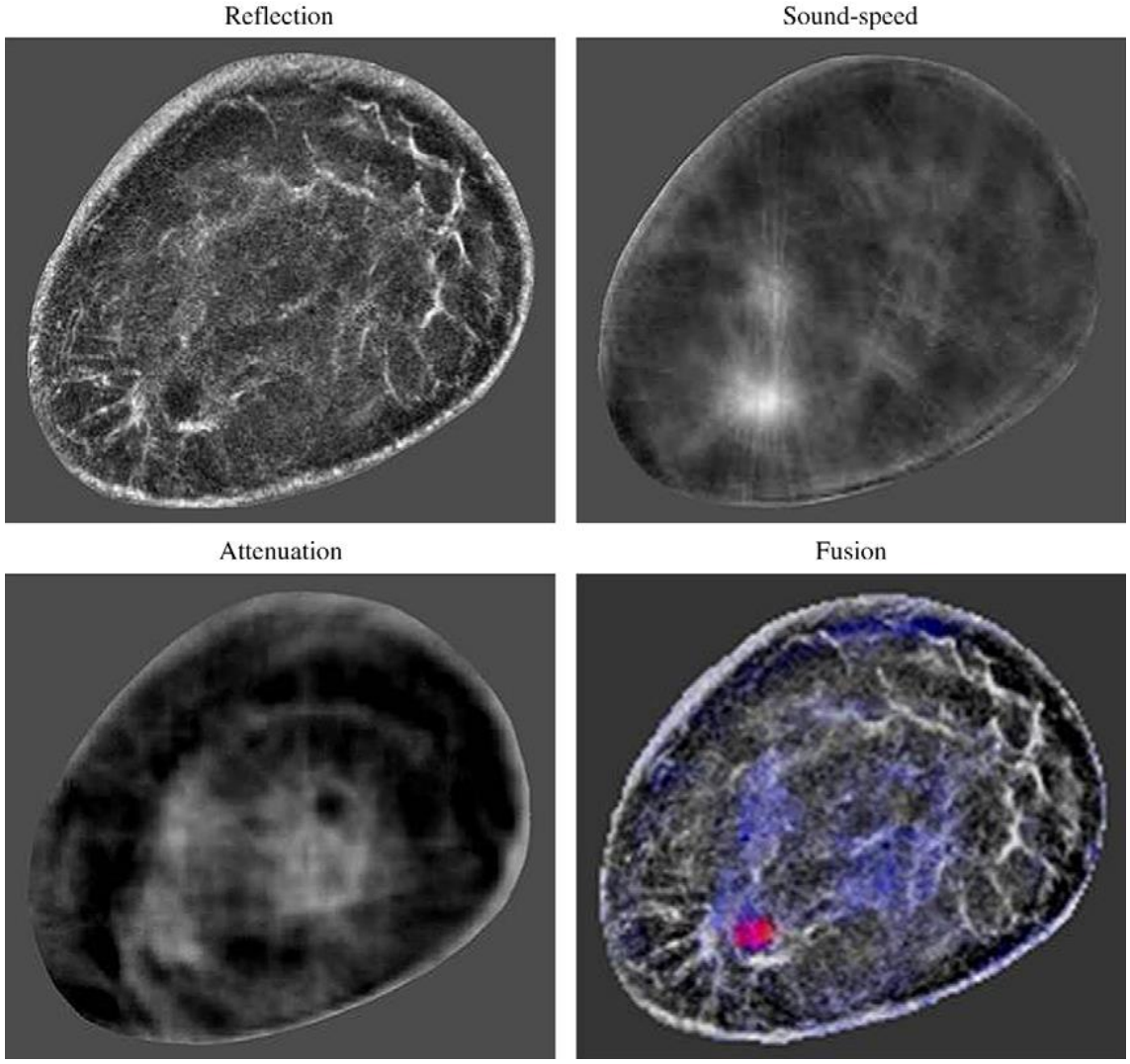

Figure 6: The CURE system records produces reflection, sound-speed, and attenuation images.

Juřík *et al.* have developed an ultrasound tomography imager called the Karlsruhe 3-D Ultrasound Computer Tomography I. Instead of imaging one section at a time, the entire specimen is imaged at once. In total, 1920 transducers are arranged on a cylinder, which is rotated through a number of positions to increase the number of angles. A true 3-D reconstruction algorithm is employed to

compute the entire volume at once, instead of a section at a time. This allows for truly isotropic spatial resolution in all directions.

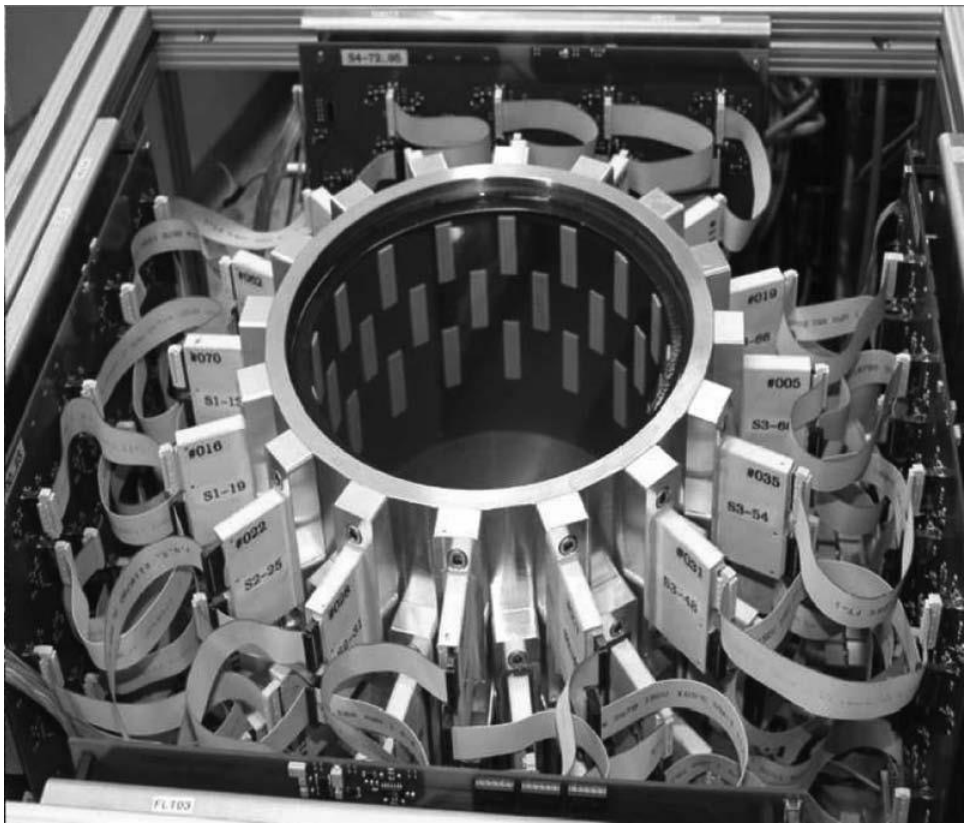

Figure 7: Three-dimensional transducer array used by the Karlsruhe system [23].

Figure 8 shows a speed of sound image taken with the Karlsruhe imager.

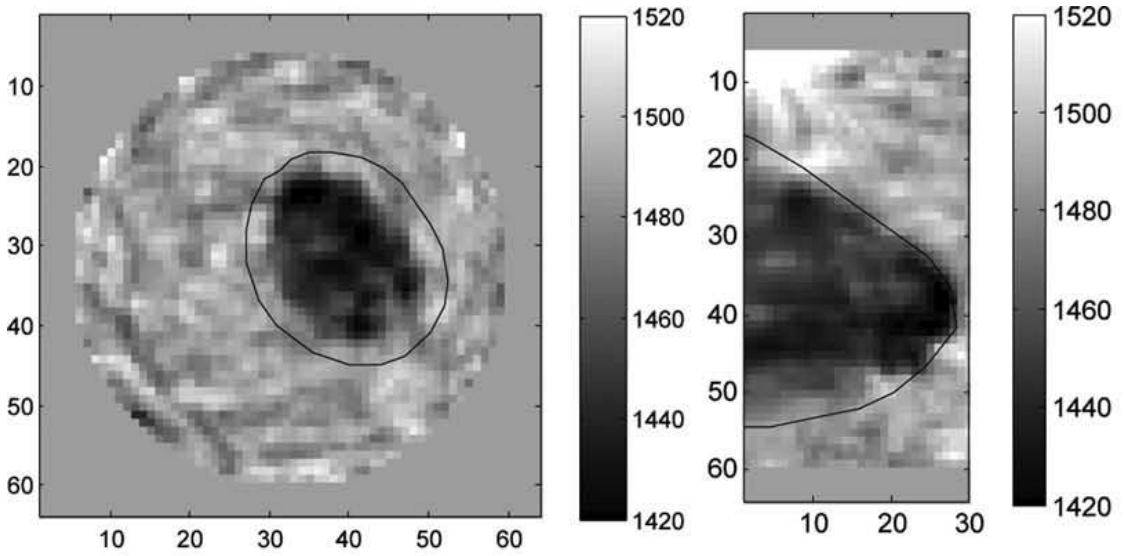

Figure 8: Two sectional images from the Karlsruhe ultrasound computed tomography prototype of a breast phantom [23].

Both the Karlsruhe and CURE systems are limited in resolution by the low number of transducer elements used in each projection. They are able to image in a reflection mode however, which allows the devices to easily resolve boundaries.

There is promise for this imaging method to be used as both a diagnostic and screening tool for breast cancer [3].

2.3.5 Speed of Sound Dispersion Imaging

Speed of sound dispersion imaging was developed by Levy and others as a new contrast source that could potentially aid in locating tissue abnormalities in the breast. In this method a pulse of two different frequencies is transmitted through the specimen: the time difference in the arrival between the two frequencies is then measured and plotted with scan position. Levy et al [15] used frequencies of 1 and 2 MHz to demonstrate this effect in a breast phantom, polyvinylchloride, and bovine myocardium. As water is non-dispersive, it does not create contrast in the image – however, dispersive media, such as the soft tissues of animals [15], [26], [27], do create contrast. It is hypothesized that cancerous lesions, having different

acoustic properties than their surroundings, will produce a different contrast signature and be visible in a dispersion scan. Figure 9 shows lesions in a breast phantom (arrows) that have caused the two interrogating frequencies of the wave to shift relative to one another, producing a region of differing contrast from the surrounding phantom.

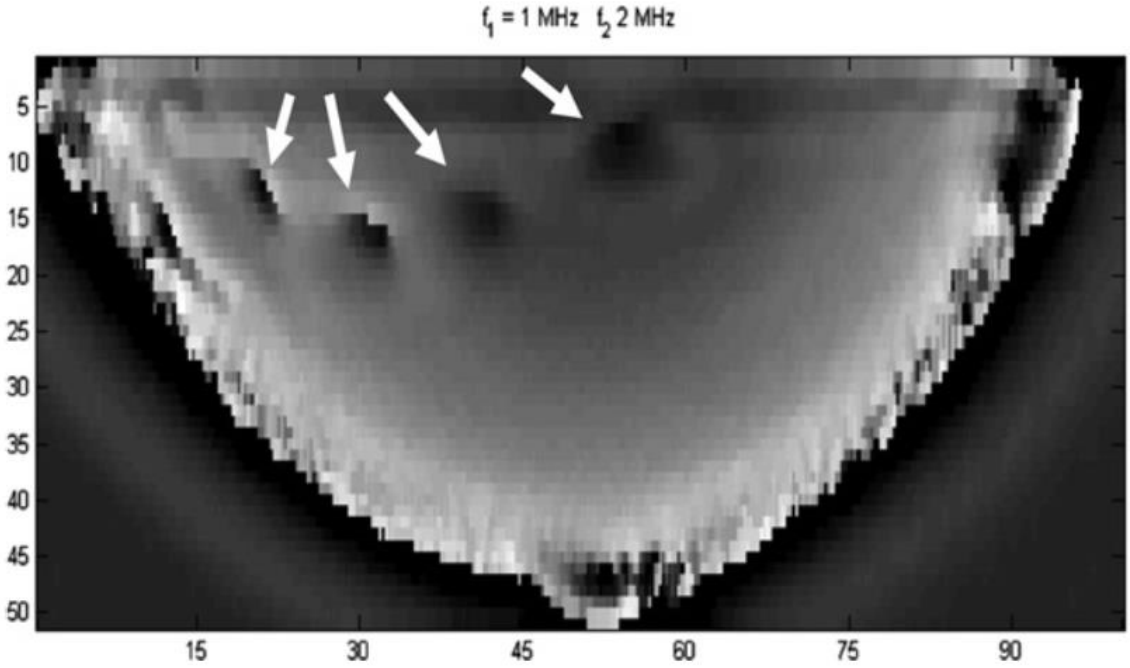

Figure 9: A speed of sound dispersion image of a breast phantom showing the total time difference between two waves of different frequencies [15].

This imaging method does not provide a measure of localized dispersion, but rather the cumulative time difference through the entire specimen. This method essentially provides dispersion projections of the specimen, and would make an ideal candidate for tomographic imaging. This idea is discussed further in Section 6.2.3.

2.4 Non-linear Bent-ray Reconstruction Methods

As tomography is adapted to different fields core assumptions made in the past no longer apply. For example, the assumption that all rays pass straight from

emitter to receiver may not accurately model the beam-specimen interaction in a specimen that causes the beam to refract (see, for example, Figure 10).

In a specimen with a heterogeneous speed of sound distribution, the beam does not pass straight from emitter to receiver: rather, it is refracted (or bent) along the way. This refraction is modeled using bent ray paths – paths that, instead of travelling straight through the object space, change direction depending on the current solution to the speed of sound distribution in the object. This approach was made popular in seismic imaging, and can be used if a high-frequency assumption is satisfied – that is, no features of interest are smaller than half a wavelength [5]. Figure 10 shows ray paths through a simulated breast phantom from two ultrasound emitters calculated using a bent-ray model. The authors note the strong refractive effects along the sides of the breast phantom due to the (simulated) subcutaneous fat layer.

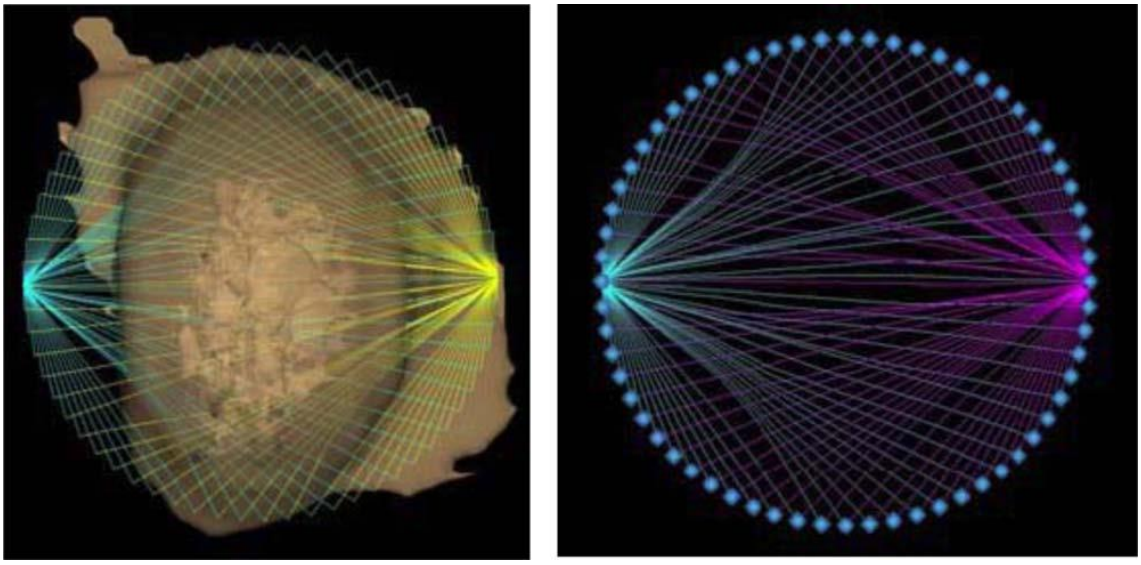

Figure 10: Bent-ray paths from two ultrasound emitters to receivers through a simulated breast phantom [5].

One method, presented by Li *et al.* [5], is based on the eikonal equation, and is derived as follows. The derivation starts with the general wave equation for an

adiabatic process, equation 18. Then, a harmonic solution is assumed, taking the form:

$$u = A(\boldsymbol{x}) \exp -i\omega(T(\boldsymbol{x}) + t) \qquad 30$$

where: u is a scalar field (i.e. pressure)
$A(\boldsymbol{x})$ is the wave's amplitude at location $\boldsymbol{x}$,
And $T(\boldsymbol{x})$ is a phase function that describes a surface of constant phase.

If this expression is then substituted into the wave equation, we arrive at:

$$|\nabla T|^2 - \frac{1}{c^2} = \frac{\nabla^2 A}{A\omega^2} \qquad 31$$

Here we apply the high frequency assumption, and the right hand side term disappears as the angular frequency ω dwarfs the normalized Laplacian of the amplitude A. We are then left with:

$$|\nabla T|^2 = \frac{1}{c^2}\ , or\ \left(\frac{\partial t}{\partial x}\right)^2 + \left(\frac{\partial t}{\partial y}\right)^2 + \left(\frac{\partial t}{\partial z}\right)^2 = U^2 \qquad 32$$

where U is called the slowness, and is a scalar function of position $\boldsymbol{x}$. This equation is most often solved using the Fast Marching Method (FMM), and was originally introduced by Sethian [28]. While this method of image reconstruction was not used in these experiments, future work should incorporate non-linear image reconstruction techniques as these methods better model wave-specimen interactions.

CHAPTER 3 – DEVELOPMENT AND OPERATION

Spatially-filtered continuous-wave acoustic tomography evolved from the development of a series of imaging devices developed at the University of Victoria under the guidance of Dr. Rodney Herring.

3.1 PREVIOUS WORK

3.1.1 CONFOCAL SCANNING LASER HOLOGRAPHY MICROSCOPE

Rodney Herring initially conceived of a Confocal Scanning Laser Holography (CSLH) microscope for the determination of the three-dimensional refractive index of fluids [29]. A CSLH microscope was successfully built and tested by Peter Jacquemin [30], who used it to measure the spatial refractive index distribution (6x8 tomogram) of a known fluid specimen around a heating element. The refractive index measurement was then used to determine the temperature distribution in the fluid from an empirical relationship. A third dimension was added by creating tomograms of successive planes parallel to the querying beam (typical of many three-dimensional imaging techniques). Figure 11 shows a schematic representation of the CSLH microscope. After the conception of the microscope, a method of creating refractive index tomograms from the holograms it records was needed.

Lai et al proposed a scanning technique and reconstruction algorithm for the CSLH microscope [31]. The algorithm involved scanning a 4x4 domain and solving successive grid cells, where the solution to the current cell relies on previous solutions. This technique was shown to work for ideal cases with no measurement errors and continuous linear or circular refractive index distributions; however,

this algorithm does not present a workable solution, as errors compound with the solution of each cell.

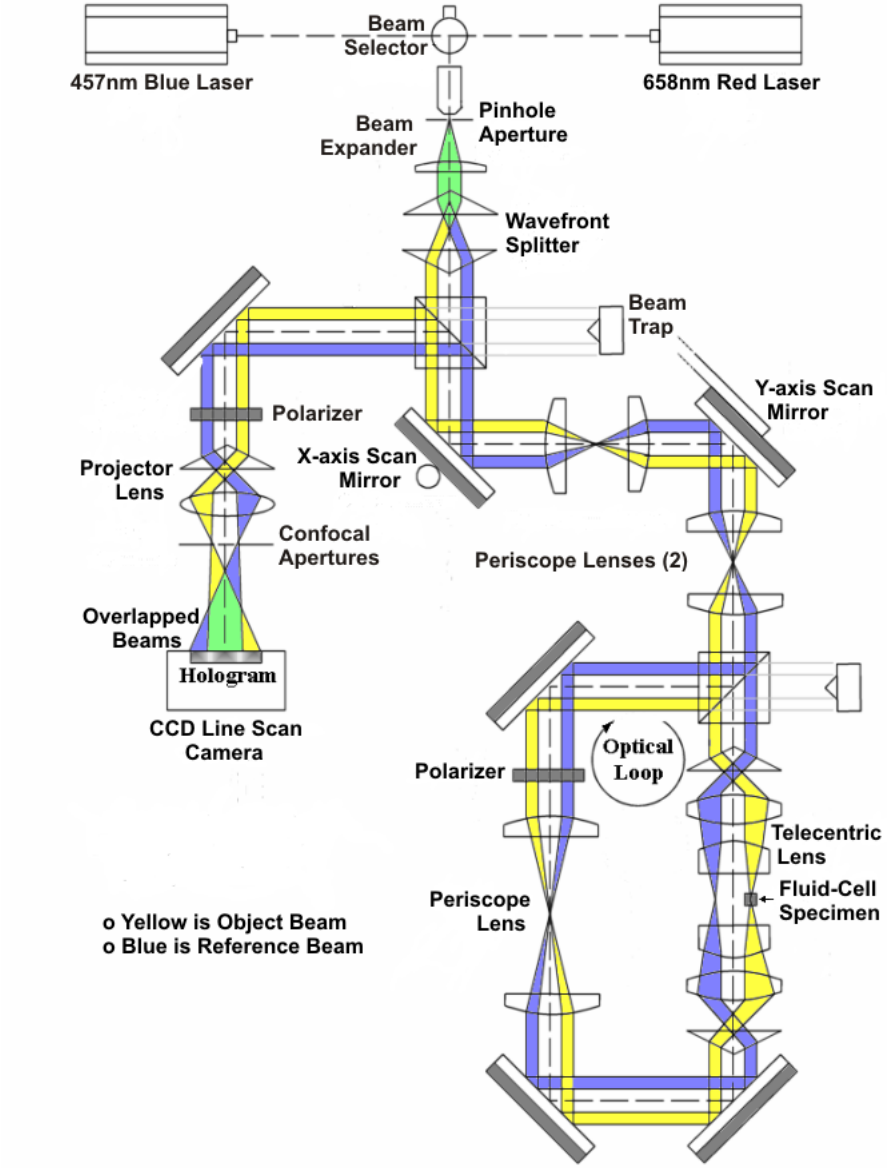

Figure 11: A confocal scanning laser holography microscope [29], [30].

While the microscope was successful, the imaging process comes with limitations. Chief amongst them is the limited view imposed by the cone angle of the confocal beam, making the determination of the refractive index distribution an ill-posed and ill-conditioned inverse problem [30]. The use of only the two marginal rays by Jacquemin in the reconstruction algorithm exacerbated this

problem, essentially limiting the number of viewing angles to two. The use of *a priori* refractive index information was needed in order to make the problem solvable: one third (or 16 of 48) of the refractive index values were assumed to be known *a priori*. This reconstruction algorithm was called the 'wily' method.

The inclusion of all rays passing through the specimen, in combination with a least-squares or other over-constrained type reconstruction algorithm would have yielded better results (thanks to the reduction in random error and the inclusion of more views); however, *a priori* information would still be required to achieve an accurate solution because of the limited viewing angle.

3.1.2 Confocal Acoustic Holography Microscope

Stefan Atalick designed, built, and tested a proof-of-concept confocal acoustic holography microscope [16], shown in Figure 12. The proof-of-concept instrument was able to measure the advancement or delay of a sound pulse that passed through a cuvette filled with a sample fluid. This was done by interfering two wavefronts: one which had passed through a reference medium, and the other which had passed through a cuvette. The shift in the resulting hologram, when compared to a previous reference hologram taken with only water in the cuvette, gave the phase change between the two cuvette paths (water and sample fluid). This phase change, along with the dimensions of the cuvette, was used to determine the speed of sound in the fluid sample.

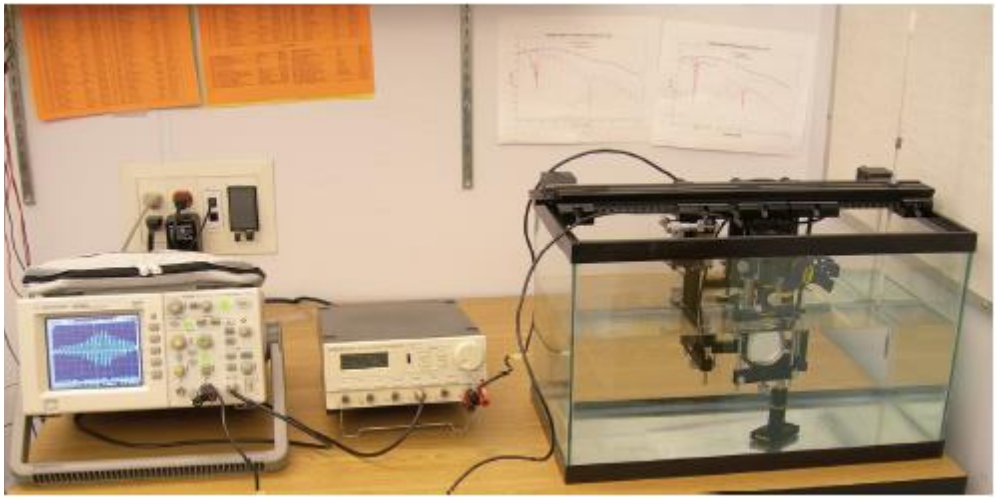

Figure 12: Experimental CAHM setup [16].

It was also proposed that the 3D speed of sound distribution of two different frequencies (essentially, dispersion) in a fluid sample might be used to determine its temperature. However, there is no known universal speed of sound - temperature - frequency relationship, making the determination of the temperature of an unknown specimen currently impossible. If the medium is exactly known, it is possible to obtain the temperature from the speed of sound using an empirical relationship (such as Marczak's equation for pure water at atmospheric pressure).

The use of a similar algorithm to that used in the CSLH (the 'wily' algorithm) was investigated for application to an acoustic device. This did not bear fruit. Wily uses an object space of 8 by 6 pixels – which is insufficient for use in a medical device. The requirement for *a priori* information was deemed unacceptable. Finally, the wily algorithm does not scale – the number of unknowns increases by the square of the number of pixels in each row while the number of equations only increases linearly. Any one of these three factors alone is enough to make the use of the wily algorithm unsuitable for application in a medical imaging device.

3.1.3 A NOTE ON HOLOGRAPHY

In traditional holography, all the information contained in the object wave is captured (hence the name: *holo* – whole *graphy* – image), including scattered waves. It is often thought that holography produces three-dimensional images; however, this is not entirely correct. When viewed with the eye, reconstructions from optical holograms (optical holograms may be reconstructed physically by illuminating them with the same reference beam they were created with) appear three-dimensional because of the stereoscopic nature of human sight. Holograms can be thought of as a means to capture all the light (or waves of any kind) passing through a viewing 'window' – this 'window' limiting the total viewing angle on the object. It is true that stereography can produce three-dimensional representations of an object (topographic maps of the earth being a good example). However, the obtainable depth resolution in a hologram (and in any imaging method) is limited by the maximum viewing angle – as the viewing angle approaches 180 degrees (or more as can be the case in tomography) the maximum obtainable depth resolution approaches the horizontal resolution. One can use fiducial markers to arrange what belongs where, but there is simply not enough information to solve for the refractive index or the absorption coefficient inside an object without sacrificing depth resolution. Further *a priori* information is necessary to solve for hidden object characteristics (as in the CSLH microscope). If one were able to capture a hologram of the object on an infinite plane, then the wave field emanating from the object could be completely reconstructed without the loss of depth resolution.

3.2 DEVICE DESIGN

Two different device designs were developed with the same end goal in mind – to create projection images of an object transparent to sound. One design

interrogates the object with a focused beam, called the "confocal" scanner, and the other with a collimated beam.

3.2.1 Design 1: "Confocal" Scanner

The confocal design is shown in Figure 14. This design uses an off-axis parabolic mirror (OAP) to focus a collimated beam at an angle of 20°, and an elliptical mirror to take the focused beam and refocus it at an aperture. The aperture removes scattered rays that do not positively contribute to the image. These mirror types were used as they perform this operation without geometric aberration. The aperture beam can then be sampled directly by a detector (as is shown) or could be re-collimated using another OAP. This design is called confocal because the aperture is placed at a secondary focal point in the same fashion as in confocal microscopy.

The confocal scanner was used to produce the experimental results shown in Chapter 5. A central ray was recorded and treated as a pencil beam during reconstruction.

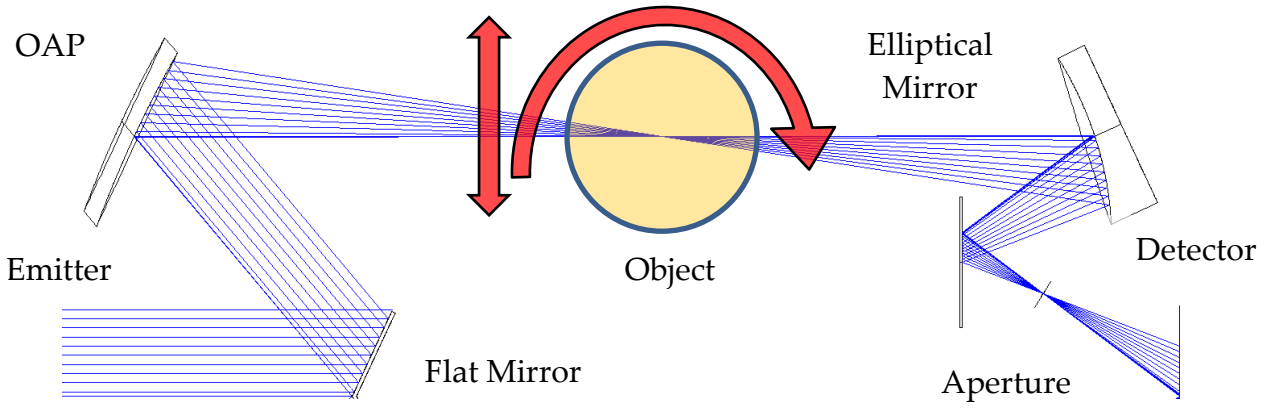

Figure 13: Confocal design.

3.2.2 Design 2: "Collimated" Scanner for Future Use

Figure 14 shows the collimated design. The collimated design utilizes two OAPs. The first focuses the roughly collimated beam coming from the emitter to pass through an aperture to spatially filter the beam. The next then re-collimates the beam, and directs it to the detector. OAPs were used in this design because they can focus a collimated beam to a point without geometric aberration, and *vice versa*. This design also negates the need to translate the object if the object is smaller than the beam diameter of the emitter. While a scanner was constructed based on this premise, no results from it are presented. This design is intended for future use.

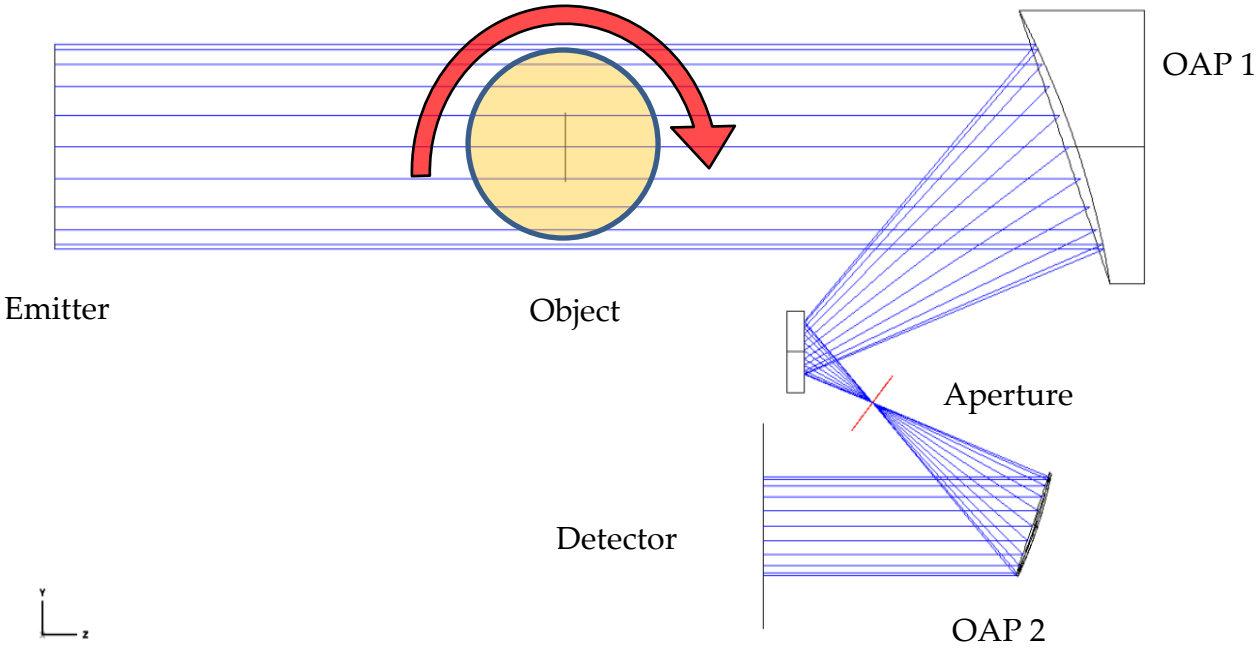

Figure 14: Collimated design.

3.2.3 ZEMAX Modeling

ZEMAX® optical design software was used to create the geometry for the proof-of-concept devices. ZEMAX uses ray-tracing algorithms to simulate the

propagation of a wave (in this case, an acoustic wave) through a medium. ZEMAX also features a powerful optimization suite, which was used to create the geometry of the acoustic mirrors. While almost exclusively used for optical design, with the change of a few parameters (wavelength and speed), ZEMAX can be used to model compression waves as well [32]. This imaging method only requires reflecting components, making the design of both tomographic scanners wavelength independent (lenses often suffer from dispersion effects - also known as chromatic aberration).

The mirrors are designed to maximize reflected intensity. Figure 15 shows the reflection and transmission coefficients at 20°C for a water-aluminum interface as a function of incident angle. All incident angles were kept above 20° wherever possible to ensure a maximum of sound energy was reflected by the mirrors.

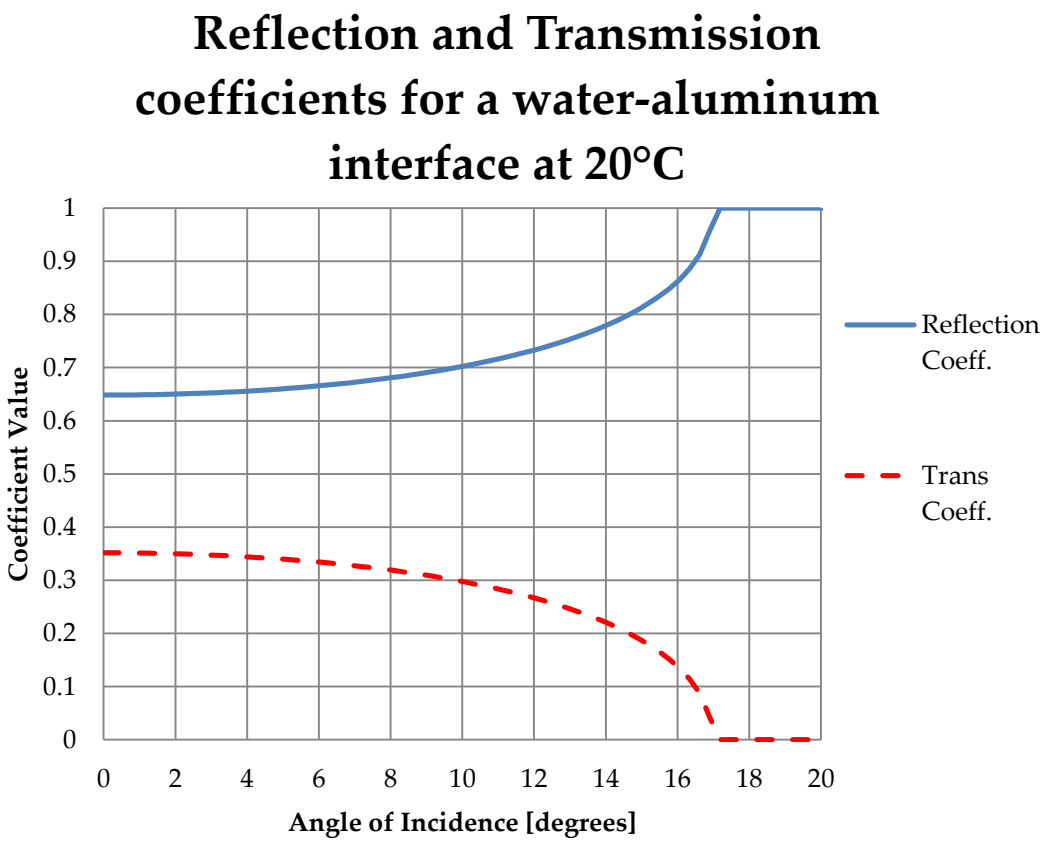

Figure 15: Reflection and transmission coefficients as a function of incident angle for a water-aluminum interface.

3.2.4 SolidWorks Modeling

After the mirrors and layout were designed in ZEMAX, they were imported into SolidWorks (Dassault Systèmes SolidWorks Corp., Vélizy-Villacoublay, France) to be developed into solid models. Mounting parts and a device assembly were also created in SolidWorks.

Figure 16 shows the SolidWorks model for the off-axis parabolic mirrors used in the collimated design. Each mirror is machined from aluminum bar stock. The non-reflecting surface of the mirror is shown as matte grey.

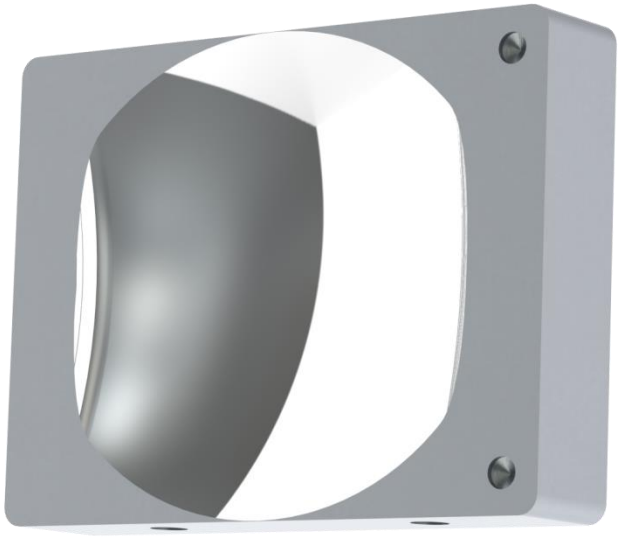

Figure 16: The SolidWorks model for the off-axis parabolic mirrors used in the collimated design.

Figure 17 shows the assembly layout of the collimated design. Mounting platforms are not shown.

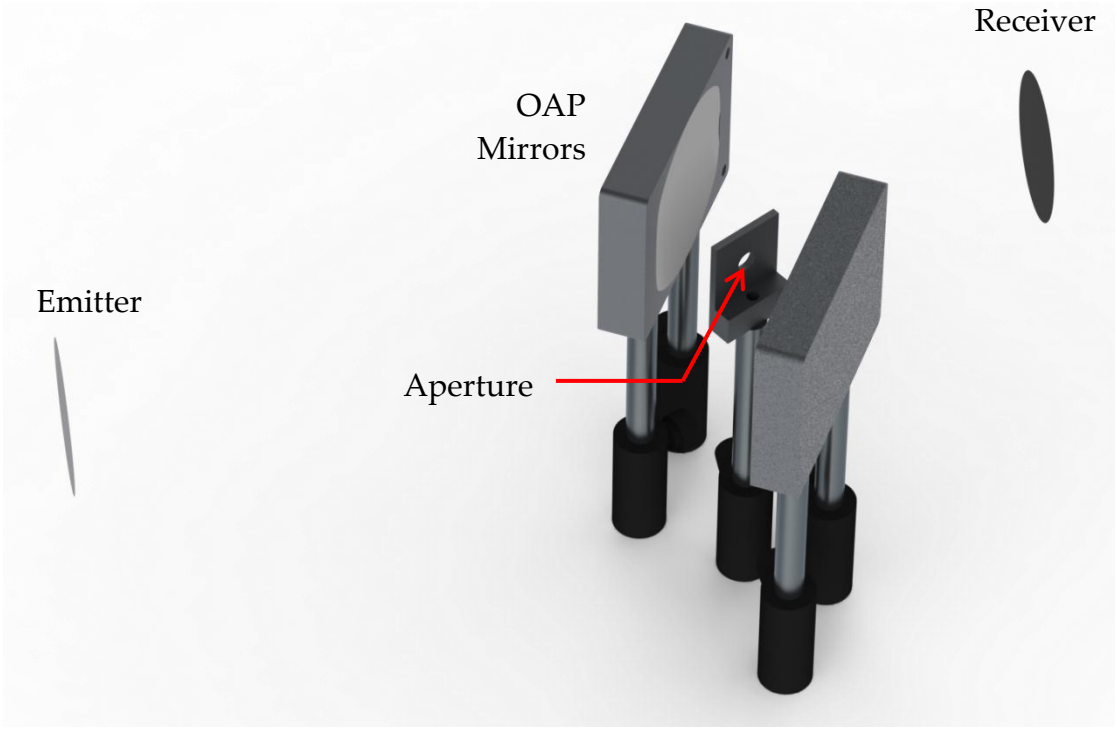

Figure 17: Collimated tomographic scanner solid model.

Figure 18 shows the OAP used in the confocal design. Each mirror features a mark to indicate its lower outside corner.

Figure 18: OAP mirror for the confocal tomographic scanner.

Figure 19 shows the elliptical mirror used in the confocal design. This mirror is significantly more dished than the others because of its short secondary focal length.

Figure 19: Elliptical mirror for the confocal design.

Figure 20 shows the confocal design assembly. The mirrors are mounted to blocks which ensure proper alignment. The blocks are then mounted on optical rail cars, which ride on an optical rail track. The rail cars must then be separated by the design distance. The aperture also sits on the mounting blocks.

After the designs were finalised in CAD, they were exported into Mastercam (CNC Software Incorporated, Tolland, CT) CAD/CAM design suite. The solid models were then transformed into machine code to operate a CNC mill. The mirrors were machined from 6061-T6 aluminum. This work was done in the department machine shop.

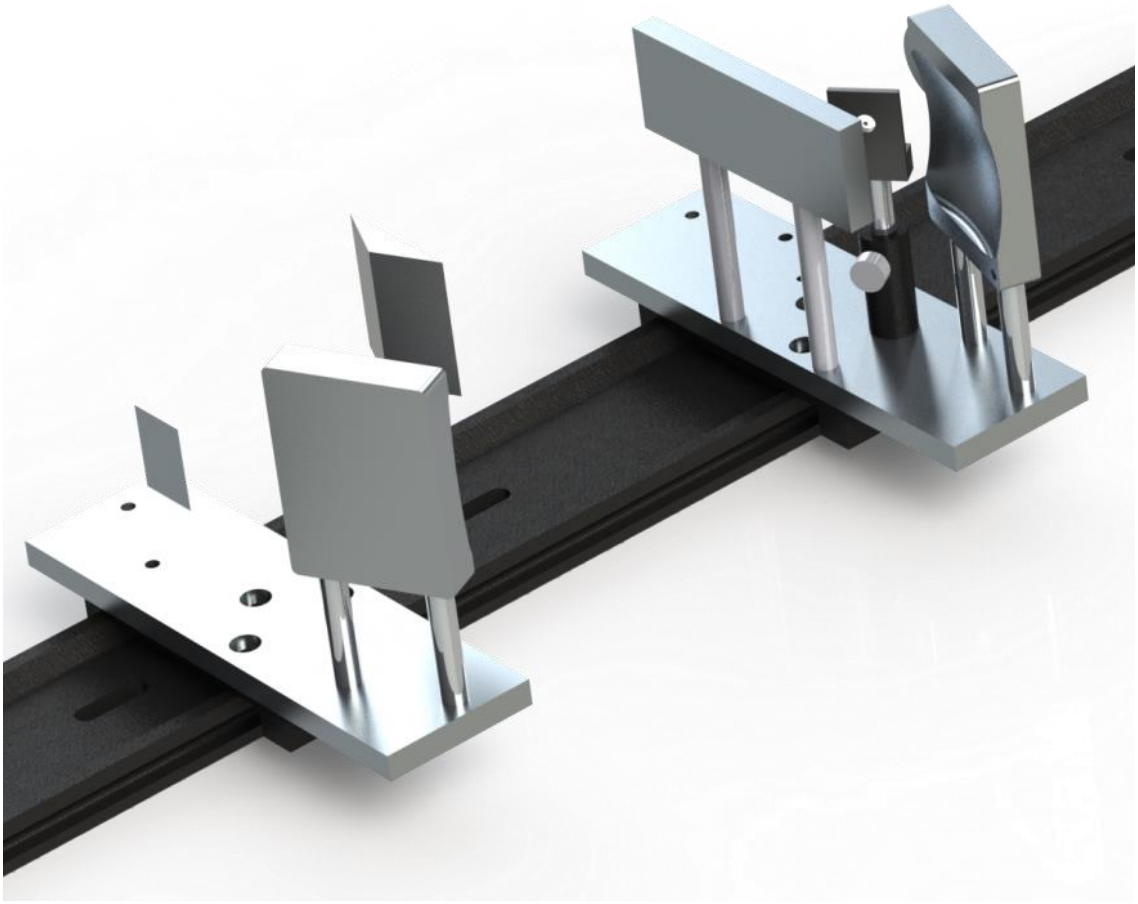

Figure 20: Solid model assembly of the confocal design. Mounting plates and an optical rail are used to secure the components.

3.3 PHASE DETECTION

The phase of the wave incident on the detector is determined in order to find the relative time of flight of the wave through the specimen. Originally, the imaging method relied on the interference of two waves travelling different paths: one travelling through the object, and another travelling through a reference (water). The interference pattern of these waves was then recorded and compared to a reference interferogram, giving the phase of the object wave. While effective, this process proved very slow, requiring an interferogram containing at least 64 points

to be recorded for every pencil beam through the specimen. A new method was developed in order to be able to determine the phase of the object wave at a point.

The continuous-wave phase determination method requires the driving function (generated by a function generator) to be concurrently recorded with the signal coming from the detector. The phase of the signal from both detector and emitter is determined using Fourier analysis, aided by the input of the driving frequency into the GUI from the user. The algorithm searches for the Fourier coefficient with the maximum value in a window defined by the user. The magnitude and angle (or phase) of this coefficient is then computed for both signals. The phase difference between the driving and received signals is recorded and stored for further analysis, along with the magnitude of the signal at the receiver. Figure 21 shows a simplified schematic of the electrical circuits used to record the emitter and detector signals.

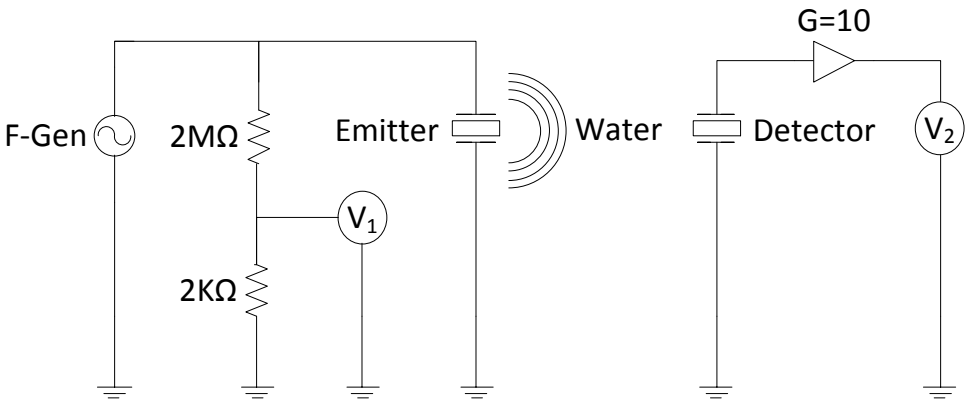

Figure 21: Electrical Schematic for recording the emitter and detector signals.

Figure 22 shows the process used to determine the phase difference between the emitted and detected signals. Typical frequencies used to drive the emitter are around 1.5 MHz, while the sampling rate of the ADC is 125 kHz.

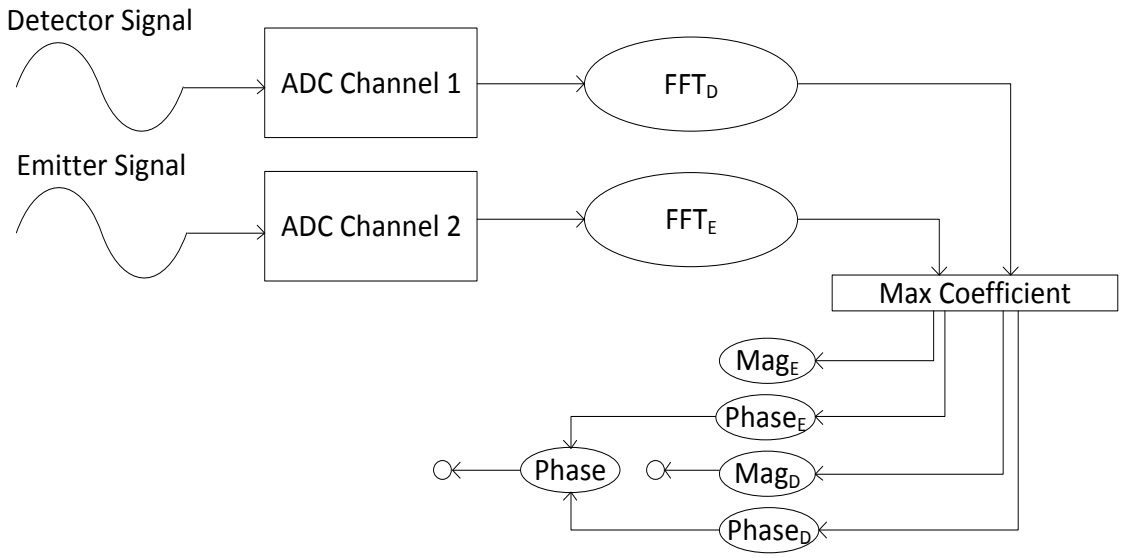

Figure 22: Process used to determine phase difference between the detector and emitter signals.

3.3.1 SIGNAL ALIASING

The Data Acquisition system (DAQ) employed in the tomographic scanners is capable of sampling 2 channels at 125 kS/s each (see section 4.3 Computer and Data Acquisition), but the signals it must capture are in the low MHz range. There is an undersampling of the signal, which results in an aliased signal being recorded. However, the user knows the frequency (or frequencies) the signal generator is creating, and therefor knows what the aliasing frequency will be. Moreover, an undersampled waveform can only undergo a 0° or 180° phase shift [33] and will have little loss in signal power. This negates the need for sampling above the Nyquist rate (twice the highest signal frequency), and is only possible in a continuous wave scheme (low frequency sampling in a pulse scheme would lead to a loss in wave arrival accuracy). Longer sampling times improve the accuracy of the measurement. Figure 23 shows how the frequency of a signal changes as a result of undersampling. Below the Nyquist frequency, the apparent and actual frequencies are the same. Above this limit, the actual frequency is aliased to a lower frequency.

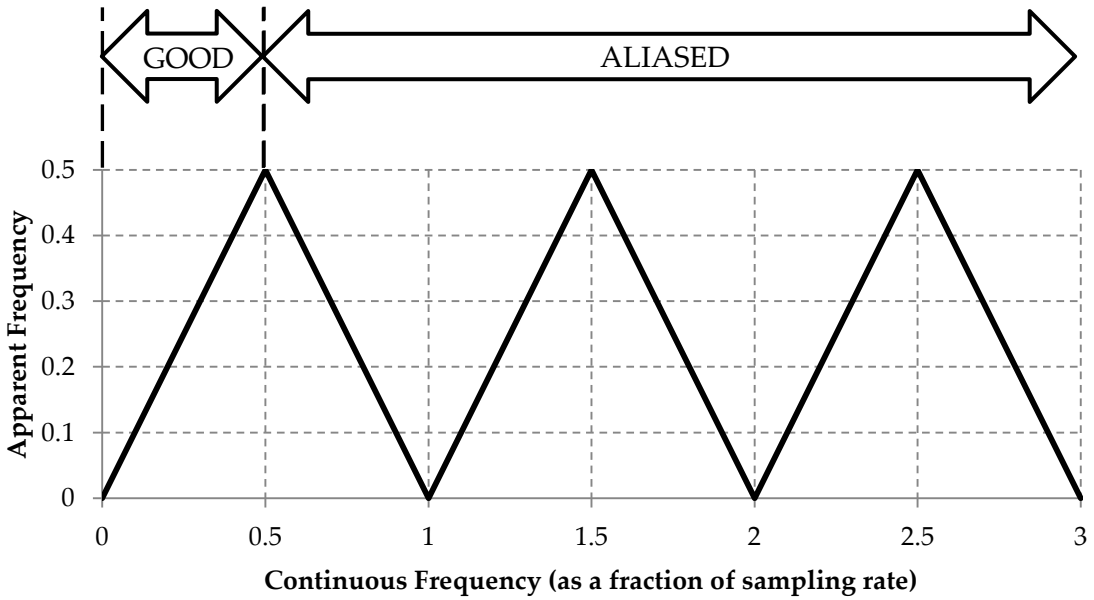

Figure 23: Conversion of actual frequency to apparent frequency.

Figure 24 shows how the phase of a sampled wave form changes with the sampling rate.

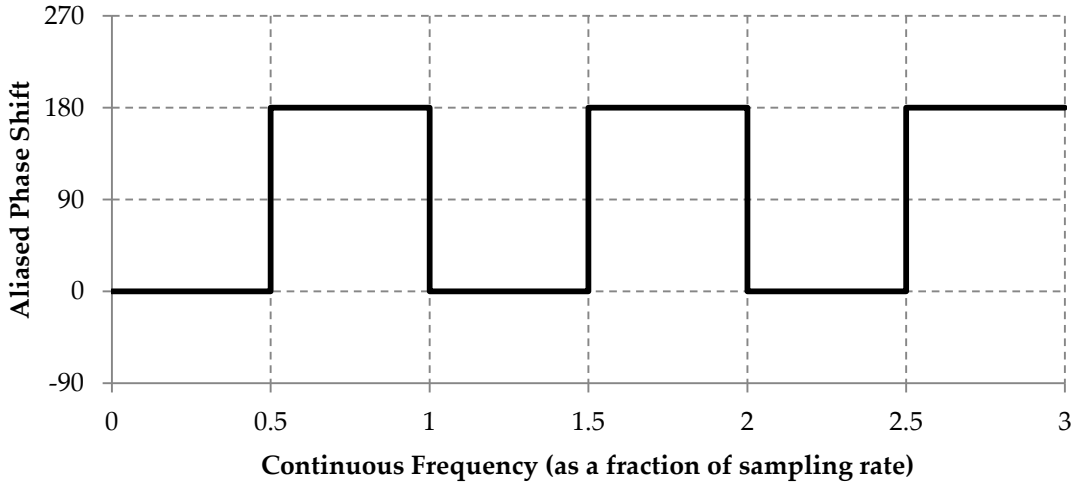

Figure 24: Phase shift of the apparent frequency due to undersampling.

3.3.2 PHASE UNWRAPPING

The phase data recorded by the tomographic scanners can only assume a value range of $-\pi$ and π. This corresponds to the phase change in one complete wave.

After this, the apparent phase resets, as wavefronts are indistinguishable from one another. This leads to a phenomenon known as phase wrapping, where successive multiples of 2π are removed from the phase value. Figure 25 shows a wrapped phase plot from one projection – the phase 'jumps' by a value of -2π from pixel 29 to 30, jumps back at pixel 33, and returns to the lower value at 34. Phase unwrapping must be carried out to correct for this.

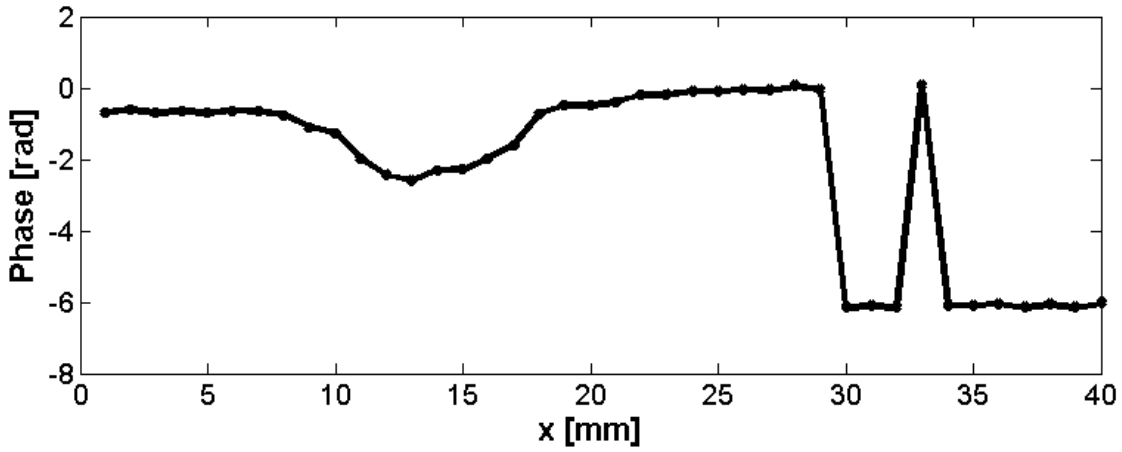

Figure 25: A 'wrapped' phase projection along one slice in y.

A simple phase unwrapping algorithm is employed by detecting jumps of greater than $|\pi|$, and then adding multiples of $\pm 2\pi$ until the gap is less than π. More complex algorithms for two-dimensional data sets utilize Green's theorem to unwrap phase images [34], [35]. Figure 26 shows the same data set, but with unwrapping applied.

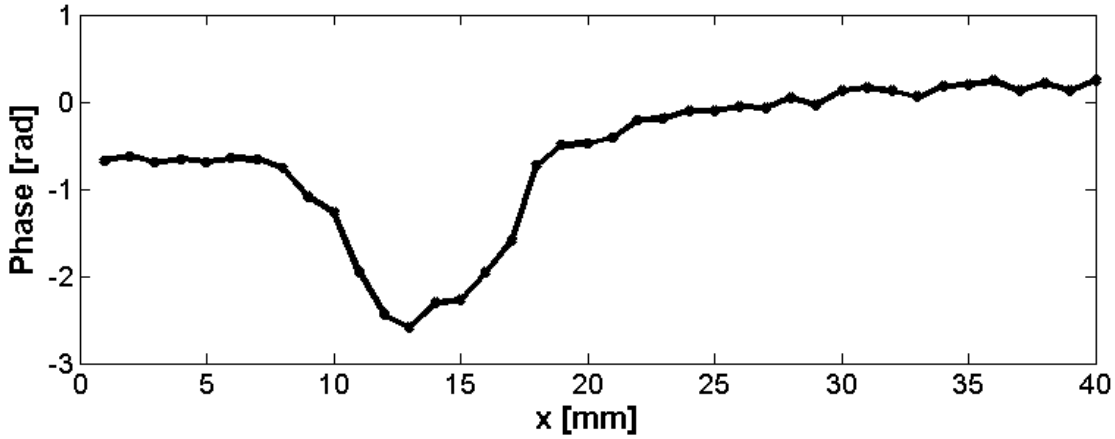

Figure 26: An 'unwrapped' phase projection along one slice in y. Jumps of ± π have been removed.

From Figure 26, we can see that there are no longer any discontinuities between points in the set. The simple algorithm employed here works well when the data points are numerous enough to capture any large changes in the phase, or when the object does no feature any sharp discontinuities that might cause a phase change of greater than π.

Goldstein's unwrapping algorithm or other advanced unwrapping algorithms should be used in future work.

3.4 IMAGE RECONSTRUCTION

3.4.1 APERTURE

Both designs feature a post-specimen aperture. This aperture is intended to act as a spatial filter, eliminating any scattered or errant sound waves that might affect image quality. Figure 27 shows a scattered sound ray being improperly focused and rejected by an aperture placed at the secondary focal point in the confocal design. In the confocal design, this aperture is seen as being virtually placed at the focal point inside the specimen (even though it filters rays that scatter after the specimen focal point). In the collimated design the aperture can be thought of as eliminating any rays which do not emanate from the virtual focal point at infinity.

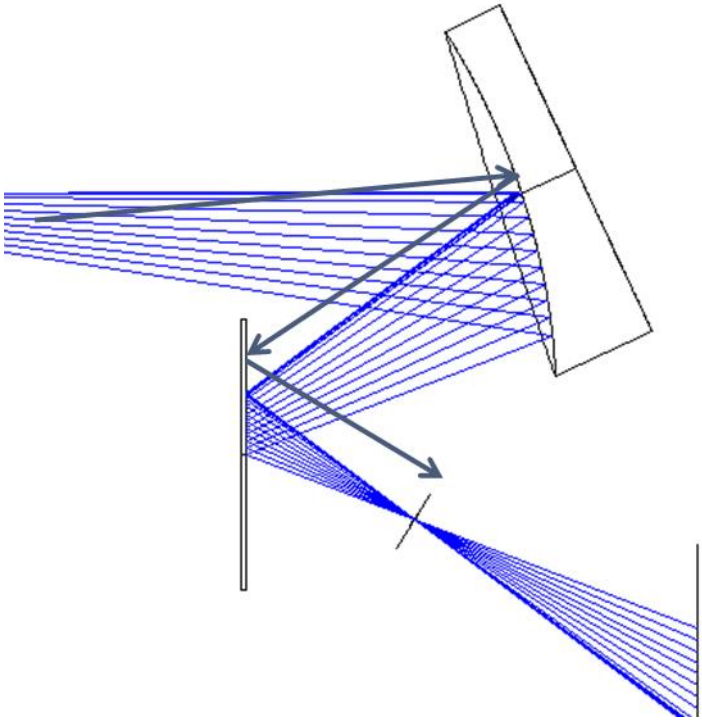

Figure 27: The aperture acts as a spatial filter, eliminating any scattered sound rays.

The inclusion of these heavily refracted or scattered rays would lead to a decrease in signal to noise ratio as well as a confusion of the phase and amplitude of the transmitted wave due to interference effects.

3.4.2 Choosing a Reconstruction Algorithm

A comparison of a number of different linear tomographic image reconstruction techniques was carried out in order to determine which method might give the best results with the parameters to be used in the imaging of a prostate phantom (see Section 4.8.1). To test the algorithms, a sample problem was created that would simulate the data sets obtained from the experimental set-up of the tomographic scanners. A Shepp-Logan head-type phantom was chosen as the test subject, and can be seen in Figure 28 under 'Original Image'. Four algorithms with different parameters were chosen: a modified least squares algorithm ("LS"), with relaxation parameters λ of 0.2 and 1; a filtered back projection ("FBP") algorithm,

where the filter (Shepp-Logan) is applied in Fourier space with spline interpolation between data points; a filtered SVD algorithm, with k = 1800 and 2600; and a modified Landweber SIRT algorithm. See section 2.1 for a description of each algorithm. The modified Landweber algorithm used was as follows:

$$\boldsymbol{m}^{k+1} = \boldsymbol{m}^{k} + \lambda \boldsymbol{G}^{T}(\boldsymbol{d} - \boldsymbol{G}\boldsymbol{m}^{k}), \qquad \lambda = \frac{2}{\sigma_1^2 + l} \qquad 33$$

where: σ_1 is the largest value in the singular value matrix of $\boldsymbol{G}$, and l is an arbitrary constant.

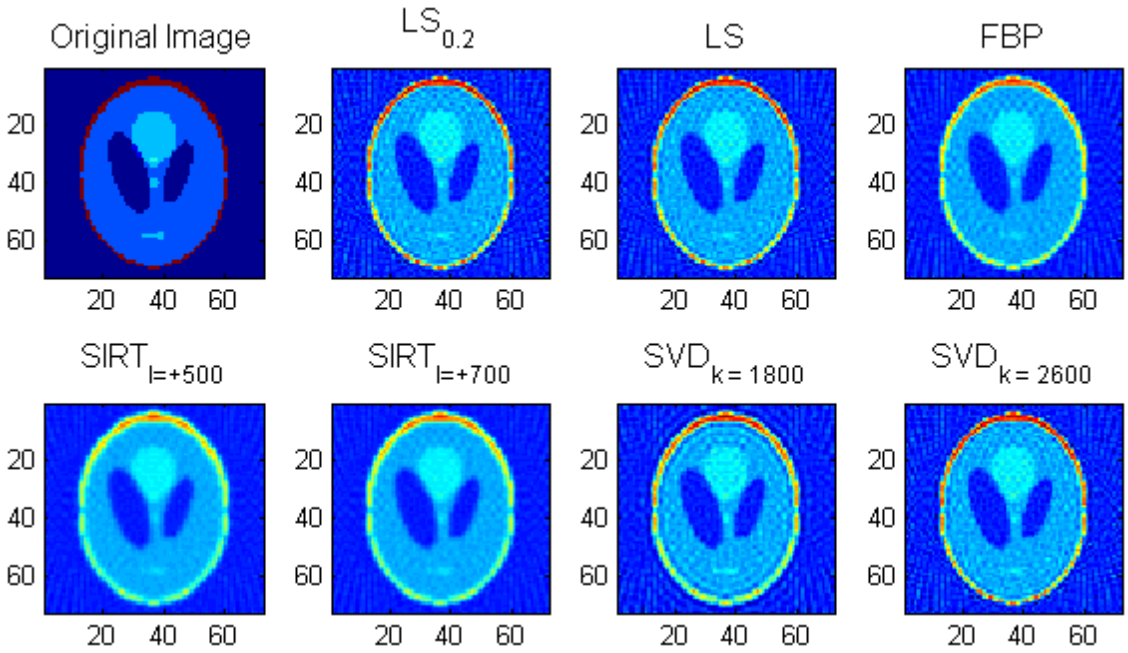

Figure 28: Performance of different reconstruction algorithms for 41 evenly-spaced angles over 180 degrees with a signal-noise ratio of 20.

Table 4 shows the performance of each algorithm in terms of accuracy and time to compute. The average error of each pixel was found by taking the difference between the sum of the values from the original phantom and the reconstructed image. This value was then divided by the number of pixels. The computation time of each algorithm is compared to that of the filtered back projection algorithm. For least squares type algorithms the computation time does not include the time

required to compute the inverse least squares matrix, as this matrix is data independent and can be computed beforehand and used for all problems with the same imaging geometry. The same applies to the SVD algorithms – the time required to do the singular value decomposition of the geometry matrix is not included, as this can be computed prior to data acquisition.

Table 4: Performance of different reconstruction algorithms for the problem in Figure 28.

Algorithm	Avg. Abs. Error / Pixel E-3	Relative Computation Time
LS $\lambda = 0.2$	5.74	0.38
LS $\lambda = 1$	5.69	0.38
$FBP_{Shepp\text{-}Logan}$	7.73	1
SIRT $l = 500$, k = 30	11.26	80.6
SIRT $l = 700$, k = 30	9.95	107
SVD k = 1800	9.21	0.72
SVD k = 2600	5.73	0.91

From Table 4, we can see that the 'LS $\lambda = 1$' algorithm performs the best, both in terms of computation time and error. This result is to be expected as this algorithm was explicitly designed to handle Gaussian noise.

The 'SVD k = 2600' performs next best in terms of accuracy, but is slower than the least squares family. This algorithm performs better and better as the signal to noise ratio is increased (decreasing noise), even surpassing the least squares solution. This is because the data set is no longer dominated by Gaussian noise. Instead, it is dominated by the aliasing effects of incomplete sampling, as only 41 angles were used.

The SIRT algorithms take a relatively long time to compute: this is because they work on the data set, so no computational work can be carried out beforehand.

They are also relatively hard to tune compared to the others, as both the number of iterations and the relaxation parameter affect accuracy.

The filtered back projection solution is quick (no pre-imaging computation required), but is not as accurate as either SVD or least squares. Other filters (Hamming, Hann, Ram-Lak) produced less accurate results than the Shepp-Logan filter result presented in Table 4.

From the results presented in Table 4 the LS λ=1 reconstruction algorithm was chosen for the tomography experiments performed in Section 5.4. It is assumed that any recording errors will be Gaussian in nature.

3.4.3 From Phase to Speed of Sound

This imaging method does not record the speed of sound of the specimen directly; rather, it determines the phase shift in the interrogating beam caused by the object. From this, a measure of the total number of wavefronts (or fraction thereof) that the object has caused the beam to shift by can be determined, and in turn the total time difference between a wave that had only passed through water, and one that passed through the object. Figure 29 shows how data is processed from the object being imaged to tomograms being created.

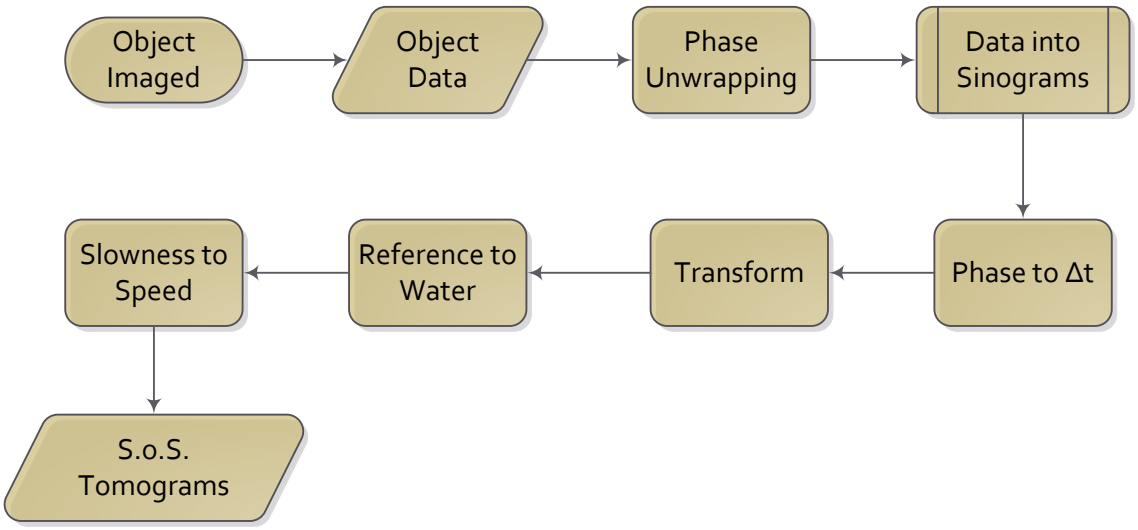

Figure 29: Data processing - from data capture to tomogram.

A spatial component is differentiated out of the time-difference value during reconstruction (as can be seen in the inverse Radon integral), leaving relative slowness [T/L] (reciprocal of speed [L/T]) values that are mapped into object space. These values are then referenced to water, and the reciprocal is taken to get the speed of sound.

3.4.4 Determining the Attenuation Coefficient

The absorbtion coefficient is used to model the loss of acoustic intensity due to non-adiabatic wave-motion (or heat loss) in a medium. Because there are also intensity losses due to scattering and the refraction and diffraction of the beam away from normal, in addition to absorption losses, the term "attenuation" coefficient is used when referring to the tomographic images of intensity loss produced by this imaging method.

Attenuation losses are modeled as follows:

$$20 \log_{10} \frac{p_1}{p_2} = \alpha s \qquad 34$$

where: p_1 and p_2 are the pressure of the wave at two points, 1 and 2,
s is the distance along the wave path between points 1 and 2,
and α is the attenuation coefficient of the medium.

Although we do not know the pressure at the receiver explicitly, we can still use this equation, in combination with the inverse Radon transform, to determine the attenuation coefficient α. If we assume that when the beam passes solely through water $p_2 \approx p_1$, the argument of the logarithm becomes the amplitude of the voltage signal generated by the receiver when there is nothing in front of the beam divided by the amplitude of the voltage signal when the object is placed in front of the beam. This is possible because the amplitude of the voltage signal generated by the piezoelectric transducer in the receiver is proportional to the applied pressure. The path length s is differentiated out through the use of the inverse Radon transform (tomographic reconstruction).

3.5 AUTOMATION

Previous iterations of the tomographic scanner were not automated – the user had to manually move the detector to capture an image. This proved to be very slow and cumbersome, and was subject to operator error (reading the position wrong). The current design is fully automated, only requiring the user to input a few initial parameters. Currently, a typical tomogram of 113 x 113 pixels taken over 41 angles takes around 75 minutes to create with a single-point detector. It is predicted that with a 64-channel piezo array detector this time will fall to 100 seconds. Further discussion of this topic can be found in Section 6.2.

CHAPTER 4 – EXPERIMENTAL APPARATUS

The hardware used to conduct these experiments consists of an arbitrary waveform generator used to generate a sine wave, motors and motor controllers used to move the object, a computer and associated data acquisition system, and an ultrasonic emitter and receiver.

4.1 ARBITRARY WAVEFORM GENERATOR

The driving signal used to power the piezoelectric ultrasound emitter is created by an Agilent 33210A Function / Arbitrary Waveform Generator (Agilent Technologies Incorporated, Santa Clara CA). The waveform generator was also used to power the emitter. The 33210A is capable of producing up to 10 MHz sine and square waveforms at 14-bit resolution and 50 MS/s.

4.2 MOTORS AND MOTOR CONTROLLERS

The proof of concept apparatus is completely automated: all motion of the specimen is conducted using linear actuators and a rotation stage. The linear actuators used to automate the apparatus are controlled using Newport Universal Motion Controller / Driver Model ESP300 (Newport Corporation, Irvine, CA). This device is connected via RS-232 to a desktop computer, which gives commands to the controller from MATLAB® (The MathWorks, Inc., Natick, MA). The controller can also be operated without an external computer via a keypad.

The rotation stage is controlled by a Mercury C-863 DC motor controller (Physik Instrumente (PI) GmbH & Co KG, Karlsruhe Germany) and is connected to the computer via RS-232.

The motors used to actuate the appartus are Newport LTA-HS stepper motors. These motors have a 50 mm stroke, and a bi-directional repeatability to 0.5 μm. The internal optical encoder gives accurate stroke position to 0.035 μm.

The rotation stage used to rotate the specimen is a PI M-037.DG. The M-037 features a 3.5 μrad minimum step, and a resolution of 0.59 μrad. The stage is capable of rotating over 360° (essentially infinite). Figure 30 shows an M-037 rotation stage.

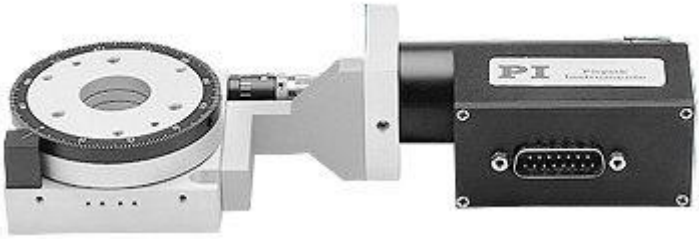

Figure 30: M-037 Precision Rotation Stage from PI.

4.3 COMPUTER AND DATA ACQUISITION

Data acquisition was provided by a National Instruments NI PCI-6221 data acquisition board (DAQ) (National Instruments Corporation, Austin TX) housed in a desktop computer running Microsoft® Windows® 7 (Microsoft Corporation, Redmond WA). Table 5 gives some of the specifications for the device.

Table 5: Analog Input Specifications for NI PCI-6221

Specification	Value
Number of AI Channels	16 (8 differential)
Sampling Rate	250 kS/s (250 kHz)
Maximum Voltage Range	-10 V, 10V
Minimum Voltage Range	-200 mV, 200 mV
Resolution	16 bit
Minimum Voltage Range Accuracy	112 μV

The DAQ does not have a high enough sampling rate to fully sample the waveform(s) produced by the emitter. The signal aliases to a lower frequency when sampled by the DAQ. The Nyquist criterion gives the aliasing frequency observed by the DAQ.

$$f_a = nf_s - f \tag{35}$$

A graphical user interface (GUI) was created in MATLAB in order to operate the motor controllers (via RS-232 communication), to control operation of the DAQ, and to record and plot data taken by the DAQ. There are multiple programs with different sampling algorithms for each different experiment. Figure 32 shows the GUI used for the dispersion tomography experiment.

MATLAB was used as the backbone for automating the imager because of its functionality, large online support resources, and the author's familiarity with the programming language.

Multiple GUIs were created to carry out different experiments. Figure 31 shows the GUI used to control the phase shift – displacement experiments.

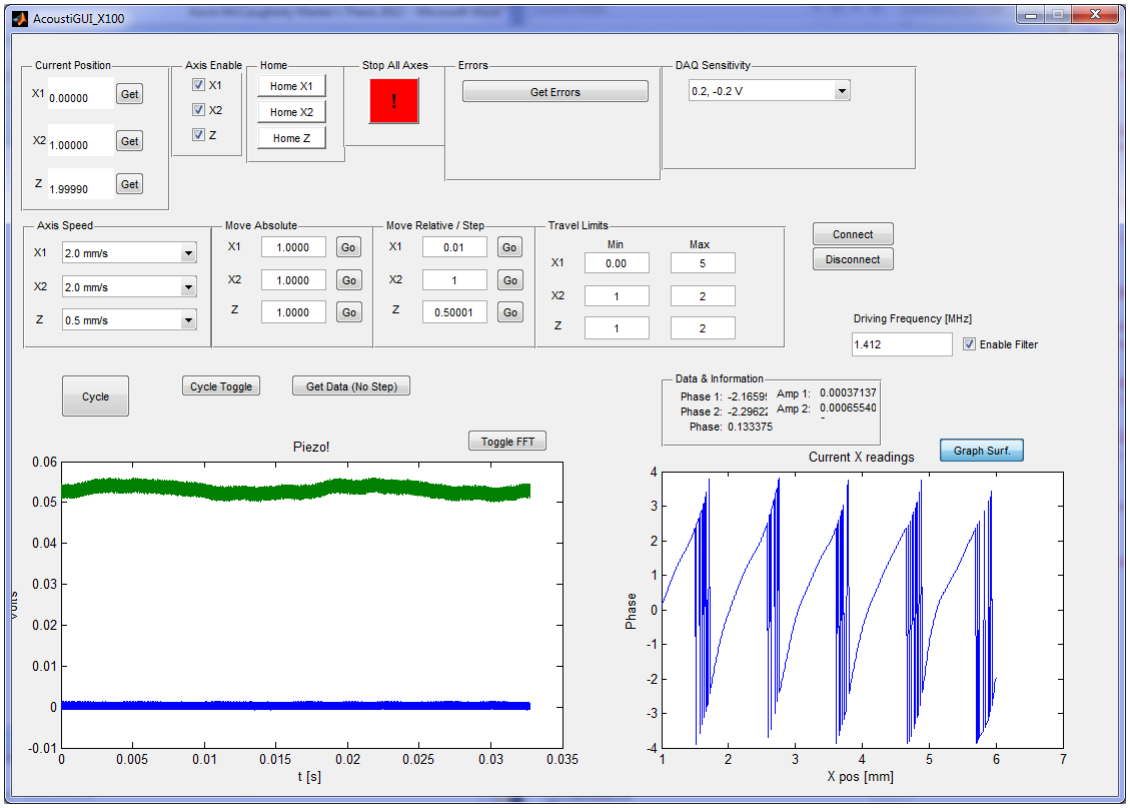

Figure 31: GUI for the phase shift - displacement test.

The phase shift – displacement GUI features a plot of the recorded waveforms and a graph showing the previous recorded phase values.

Figure 32 shows the GUI used for dispersion tomography. The functionality of this GUI is typical of most developed to automate the imaging process.

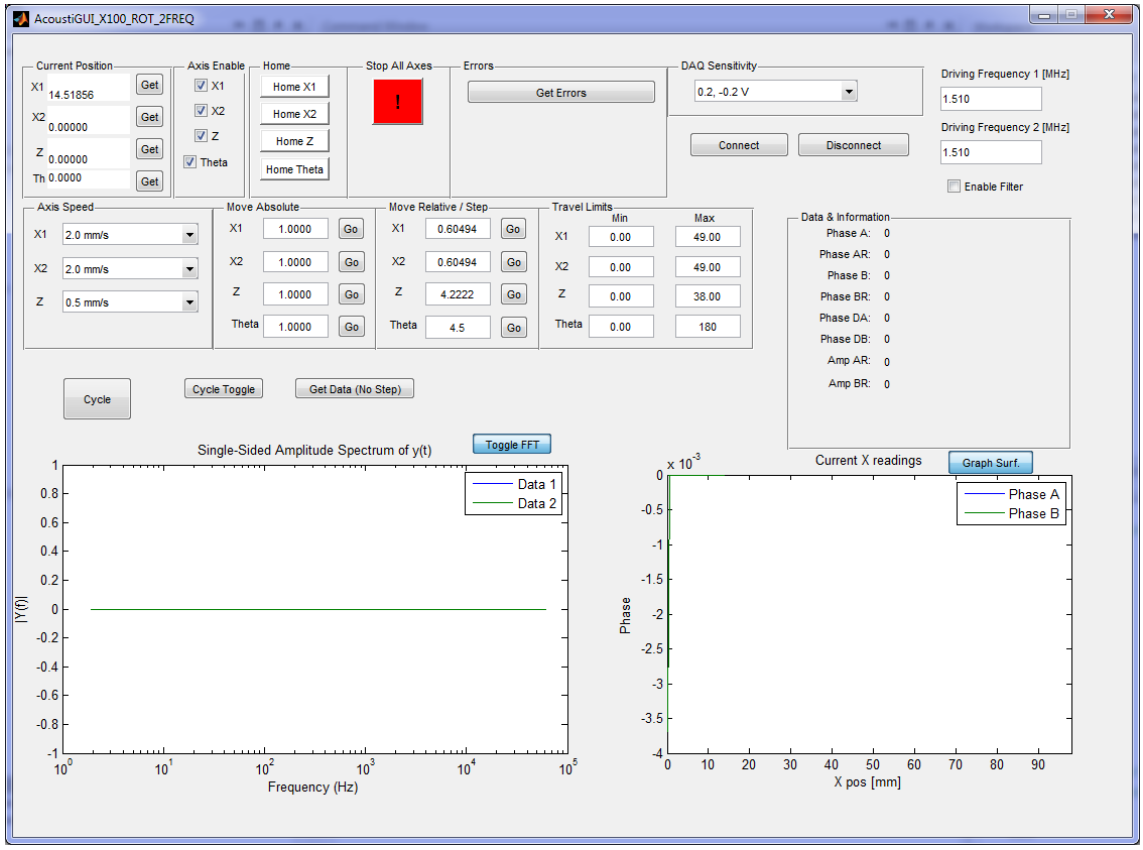

Figure 32: GUI used for dispersion imaging.

The dispersion tomography GUI has functionality for: retrieving the current axis position information from the motor controllers; enabling each axis; homing each axis; stopping all axes in the event of an emergency; retrieving and displaying errors from the motor controllers; changing the sensitivity of the data acquisition system; inputting the driving frequencies, along with an option to enable a frequency filter; setting the speed of each axis (except the rotation stage); moving each axis to an absolute position; moving each axis by an incremental value; setting the limits of travel for an imaging cycle; displaying the amplitude and phase of each frequency and waveform, as well as the phase difference between the reference and object waves; starting and disabling an imaging cycle with a soft button press; gathering one data point with a soft button press; and displaying

plots of the incoming waveforms and previously recorded data. The imaging cycle functions autonomously: user input is only required to initialize a cycle.

4.4 RECEIVER

The receiver used in these experiments was a Valpey Fisher VP-1.5R. Unfortunately, the calibration sheet for this device was unavailable to the author. Table 6 lists the specifications for this device.

Table 6: Specifications for Valpey Fisher VP-1.5R Receiver

Specification	Value
Nominal Freq.:	1.5 MHz
Element Dim.:	2.0 mm (diameter)
Focus Type:	Flat
Impedance:	500 Ω

4.5 EMITTER

The ultrasonic emitter used to produce the acoustic beam for the prototype microscope is a Valpey Fisher 5072PR ultrasonic pulser / receiver. Table 7 shows the specifications for the emitter used in these experiments.

Table 7: Specifications for Valpey Fisher 5072PR

Specification	Value
Nominal Freq.:	2.25 MHz
Element Dim.:	1.5 in (diameter)
Focus Type:	Flat
Damping:	500 Ω

This is a piezo-electric type piston transducer. This type of transducer would normally see duty in industry doing quality-control ultrasonic testing. The coating on the sensing face of each transducer is impedance matched to water.

4.6 APPARATUS ALIGNMENT

An orange laser was used as a visible means of ensuring the proper alignment of the apparatus. A beam expander was placed in the optical pathway to roughly simulate the characteristics of the acoustic emitter. An optical bench was then used to align the laser with the apparatus. Both focusing mirrors, as well as the aperture are adjustable. The alignment procedure for the confocal design outlined below can only be carried out after the apparatus has been built to initial specifications (taken from the CAD models), and represents a fine-tuning method. The apparatus was aligned in a dim room as follows:

1) The laser was turned on and directed such that the beam was parallel with the surface of the optical bench. The height of the beam was then adjusted so it struck the x = 0 plane of the microscope (or where the emitter would normally sit).
2) The parabolic mirror was adjusted such that it cast the beam on the elliptical mirror.
3) The position of the detector and aperture were adjusted such that the focal point of the elliptical mirror was at the surface of the aperture.
4) The emitter was then placed in the path of the laser, such that it's emitting face was normal to the beam.
5) Fine tuning was then carried out as necessary - both with the laser, and in the aquarium.

The difference between the path taken by the laser and the actual acoustic beam were deemed to be negligible, as a purely reflected path is independent of wavelength and wave type.

4.7 APPARATUS

The mirrors, emitter and receiver are mounted to a 100 mm optical rail (Melles Griot, Albuquerque, NM) via rail carts. The setup for the focused design is shown in Figure 33. Also shown is the rough path (red) of the acoustic beam used to interrogate the object, and a rough location of where the object would sit.

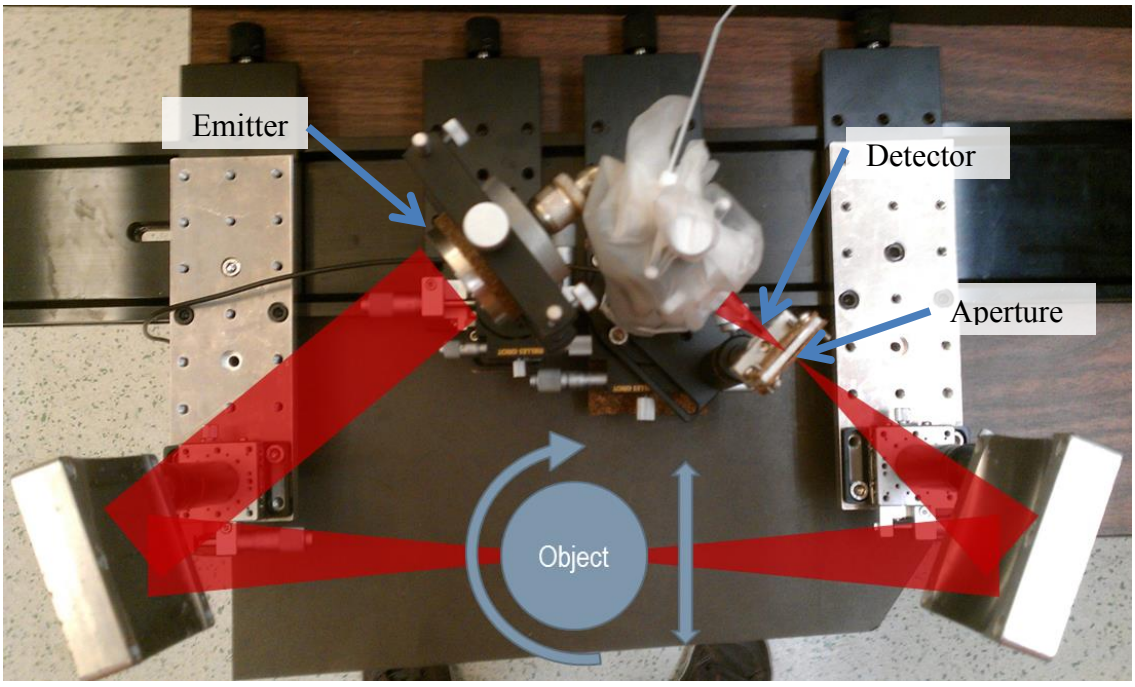

Figure 33: Experimental apparatus (focused design shown).

The mirrors, emitter and receiver are mounted to micro-adjustable bases. This allows for fine positioning during alignment. Figure 34 shows the apparatus set-up as it would be for imaging. The optical rail and components sit "up-side down" in an aquarium of water.

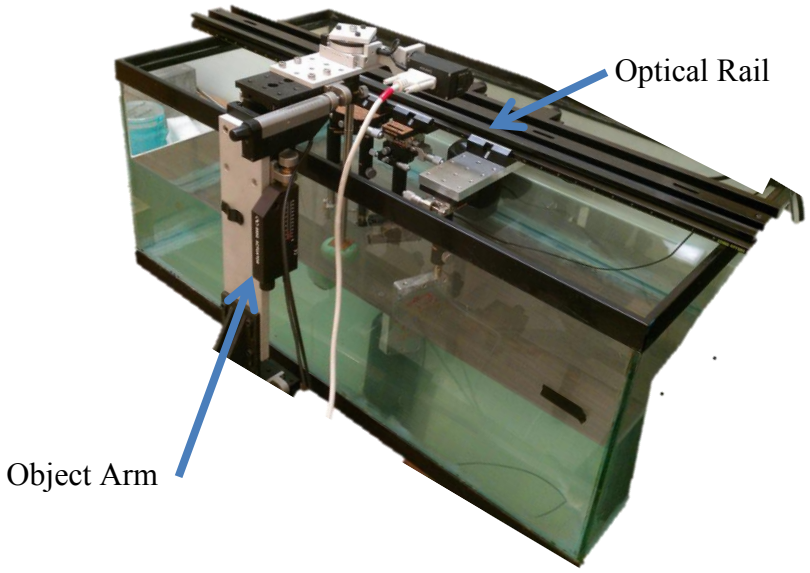

Figure 34: Apparatus in aquarium, showing object arm.

Not shown in Figure 34 are the submersed foam sheets used as sound deadening. The water / glass / air interface acts as a perfect reflector at any angle not approaching normal, and thus sound deadening was required to keep background noise to a minimum.

Figure 35 shows the object arm used to hold and manipulate the specimen. The arm has three degrees of freedom: two linear and one rotational. The object can be scanned in x and y (100 mm in x, 50 mm in y), and rotated though 360 degrees along an axis normal to beam propagation. The arm is shown here mounted to an optical rail beside the aquarium.

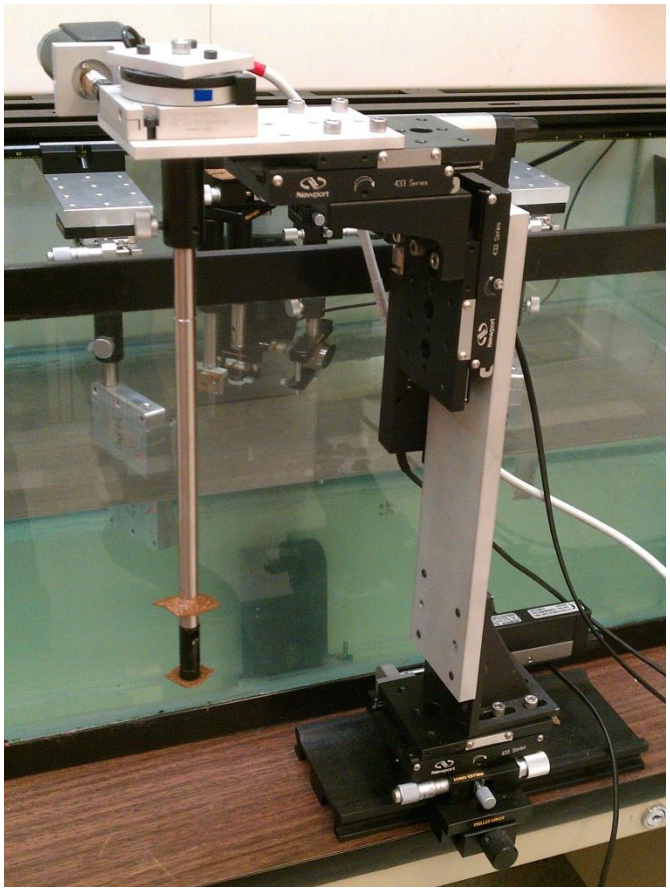

Figure 35: Object arm.

4.8 SPECIMENS

4.8.1 PROSTATE PHANTOM

An elastography prostate phantom (Model 066) was purchased from Computerized Imaging Reference Systems Inc. (Norfolk, VA) to act as a specimen for the majority of imaging tests. The phantom is made of green Zerdine® (a proprietary tissue-mimicking patented by CIRS), which has a speed of sound between 1510 and 1530 m/s. The phantom also contains three 1 cm diameter isoechoic "lesions" meant to mimic tumours. The lesions are twice as dense as the surrounding tissue. Unfortunately the manufacturer did not provide the exact speed of sound of the phantom. Figure 36 shows 3 views of the prostate phantom as it would appear before imaging. Here, it is held fast by two cork-embedded

neoprene sheets. The phantom urethra has been replaced with a low speed of sound plastic. The phantom measures 40 by 40 by 50 mm.

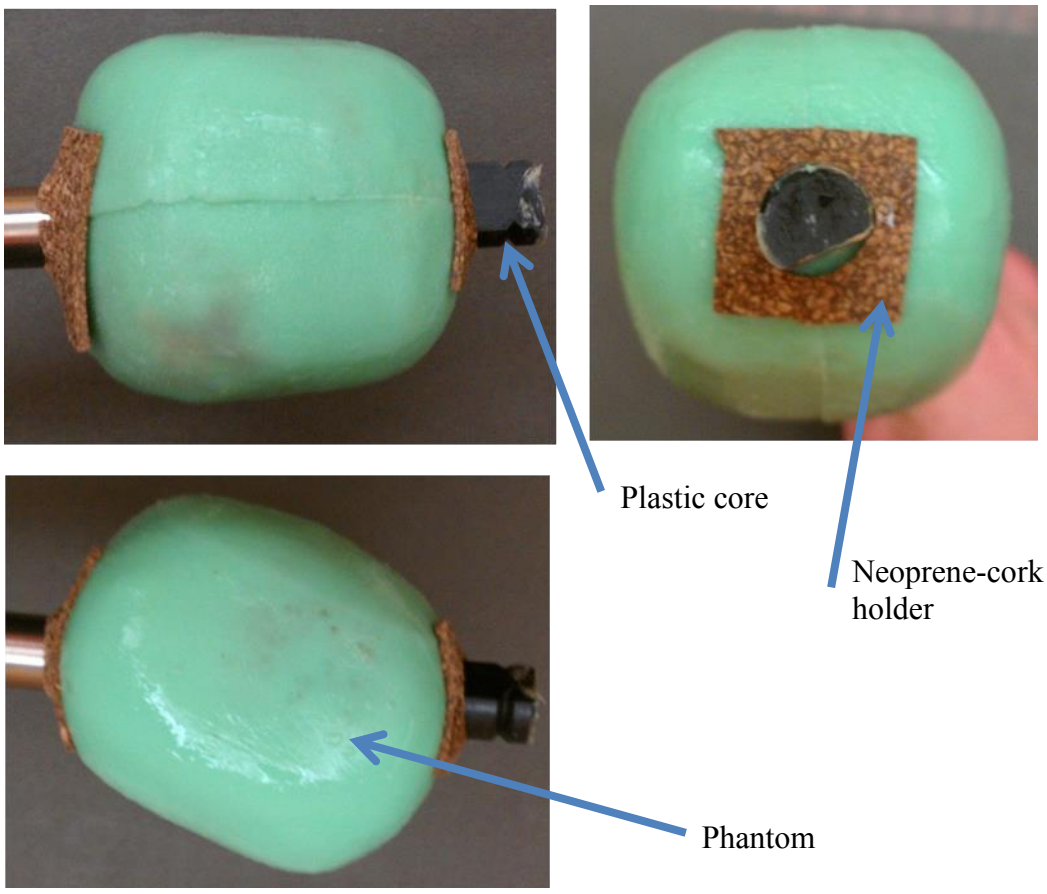

Figure 36: Prostate phantom.

The phantom had to be removed from its original housing in order to image it properly. This exposed the phantom, which is susceptible to water absorption and dissipation, to an open environment. This limited the amount of time the phantom could be continuously imaged to less than 12 hours.

4.8.2 Breast Phantom

A breast elastography phantom (Model 059, CIRS) was also imaged using the confocal tomographic scanner. The phantom contains 12 randomly positioned

high-elasticity lesions, meant to mimic breast cancer. Figure 37 shows the breast phantom.

Figure 37: Breast phantom - profile view.

Further imaging of the breast phantom will require modifications to the apparatus, as it cannot complete a full rotation without colliding with the device. The breast phantom measures 229 by 203 by 76 mm.

CHAPTER 5 – EXPERIMENTAL RESULTS

The results of an experiment devised to test the accuracy of the phase determination method is presented in Section 5.1. The experiment consists of moving the receiver away from the emitter and recording the phase of the incident wave at each point.

In Sections 5.2, 5.3, and 5.4 projection images, sinograms, and tomograms of the breast and prostate phantoms are presented. The confocal scanner was used to capture these images. Section 5.4 shows tomograms of a prostate phantom; however, the phantom should be considered *ex vivo*, as the pelvis and surrounds are entirely absent. Instead, the prostate phantom mimics imaging conditions more similar to those that might be found with a breast.

5.1 PHASE INFORMATION

An experiment was devised in order to test the ability of the data acquisition system to accurately determine the phase difference between the detected and reference signals. The data acquisition system acquired two signals: one from the waveform generator, and the other from the piezoelectric detector. The piezoelectric transducer was placed on a linear actuator and moved away from an ultrasonic emitter hooked up to the waveform generator.

The phase difference between the reference (waveform generator) and detected (piezoelectric receiver) signals should change as the receiver is moved away from the emitter. A 2π phase shift should occur over the distance of one wavelength.

The experiment was conducted using a frequency of 1.412 MHz in water with a temperature of 21.0 °C. Using Marczak's equation, the speed of sound in the tank should be 1485.409 m/s, which gives a wavelength of 1.052 mm.

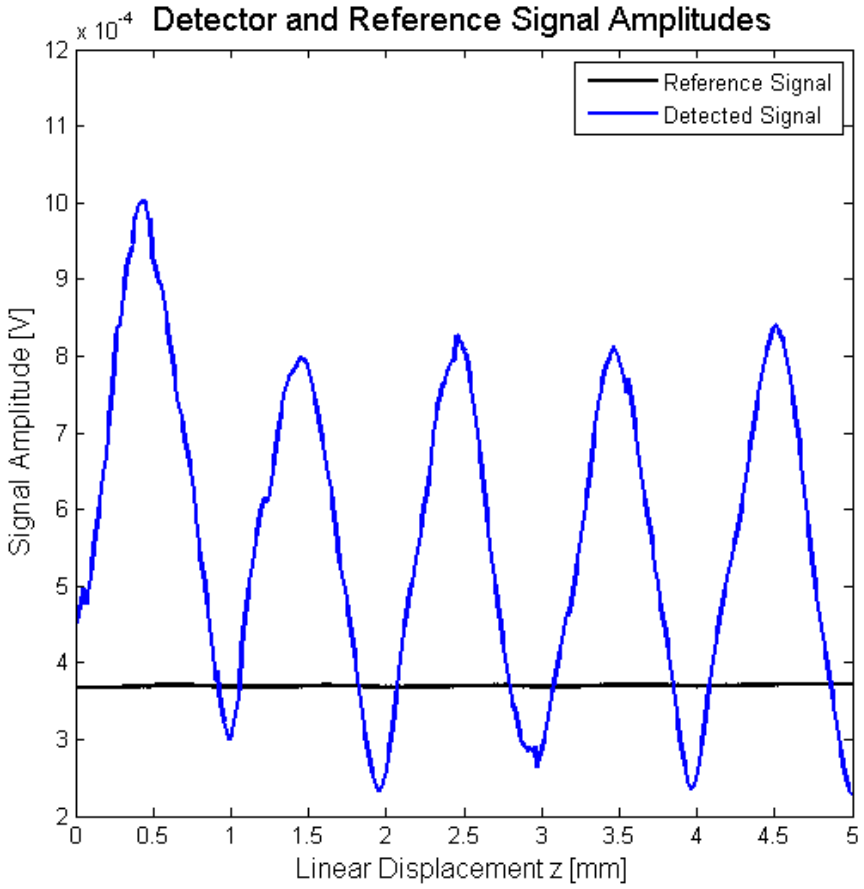

Figure 38: Detector and reference signal amplitudes for the phase-displacement test.

Figure 38 shows the amplitude of the two recorded signals. The reference signal (shown black) remains roughly constant, while the detected signal follows a sinusoidal pattern. This pattern is believed to be caused by the reflection of sound off the back wall of the tank.

Figure 39 shows the raw phase data recorded by comparing the phase of the two recorded signals. This is done via Fourier analysis. Values above / below $\pm\pi$ are a

result of the subtraction of the phase of each signal. A "sawtooth" waveform can be seen.

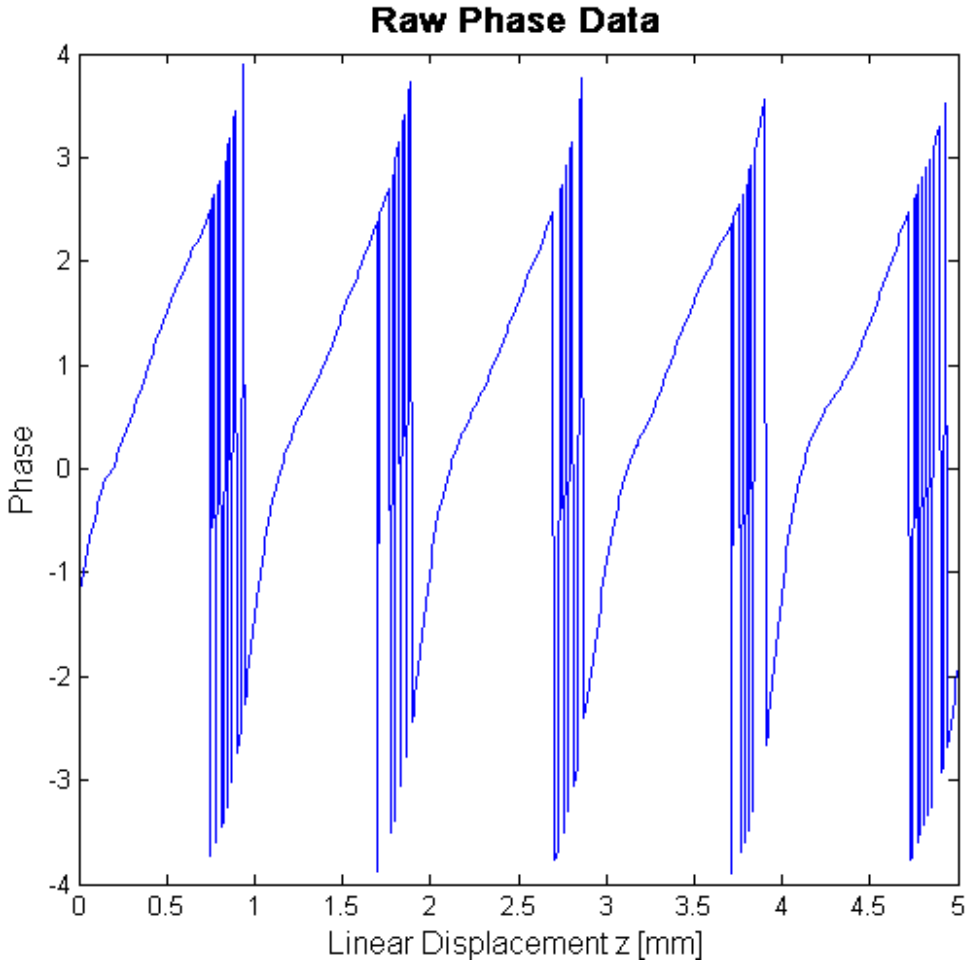

Figure 39: Raw phase data.

Figure 40 shows the corrected phase data: a limit of $\pm\pi$ has been placed on the data. From this plot we can see the phase repeats from $-\pi$ to π every 1.022 mm: an error of 2.8% from 1.052 mm.

The plot should be linear, as there is a linear relationship between phase and linear displacement. It is hypothesized that the discrepancy is a result of reflection off the end of the tank, or perhaps some electronic interference. This effect is most visible in the plot of the magnitude of the signal (Figure 38).

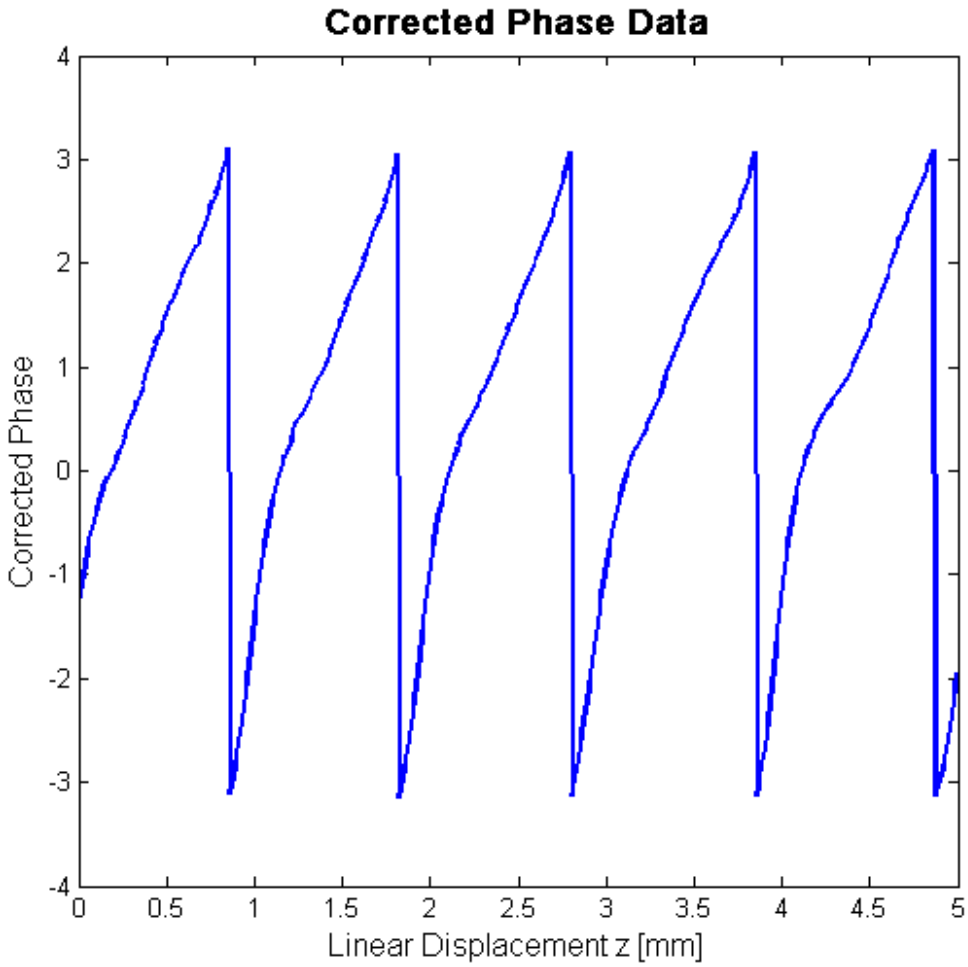

Figure 40: Corrected phase data.

This shows that using the relative phase of two signals can be used to determine the phase shift produced by an object, and through tomography, its internal speed of sound.

5.2 Breast Phantom Projections

A two dimensional projection of the breast phantom was taken using the confocal scanner. This was done by scanning the beam through the phantom in a plane normal (x-y) to beam propagation (z-axis). The phantom was stepped in 1 mm increments in both the x and y directions to produce a 40 by 40 pixel projection. The results can be seen in Figure 41 and Figure 42. The breast phantom

is too large to allow for a full tomographic scan using the current linear actuators and tank, however it proved useful in testing the fidelity of any recorded projections.

Figure 41 shows the (pixelated) outline of the breast phantom (generally light blue), its interior (dark blue), and surrounding water (yellow). Refractive effects can be seen as regions of lower / higher relative intensity - both within the phantom and at its edge. This effect is quite noticeable at the “nipple” (deep red) where the phantom has created a converging lens. The lesions inside the phantom are not visible in this projection – their effect is simply too small to be seen over the rest of the phantom.

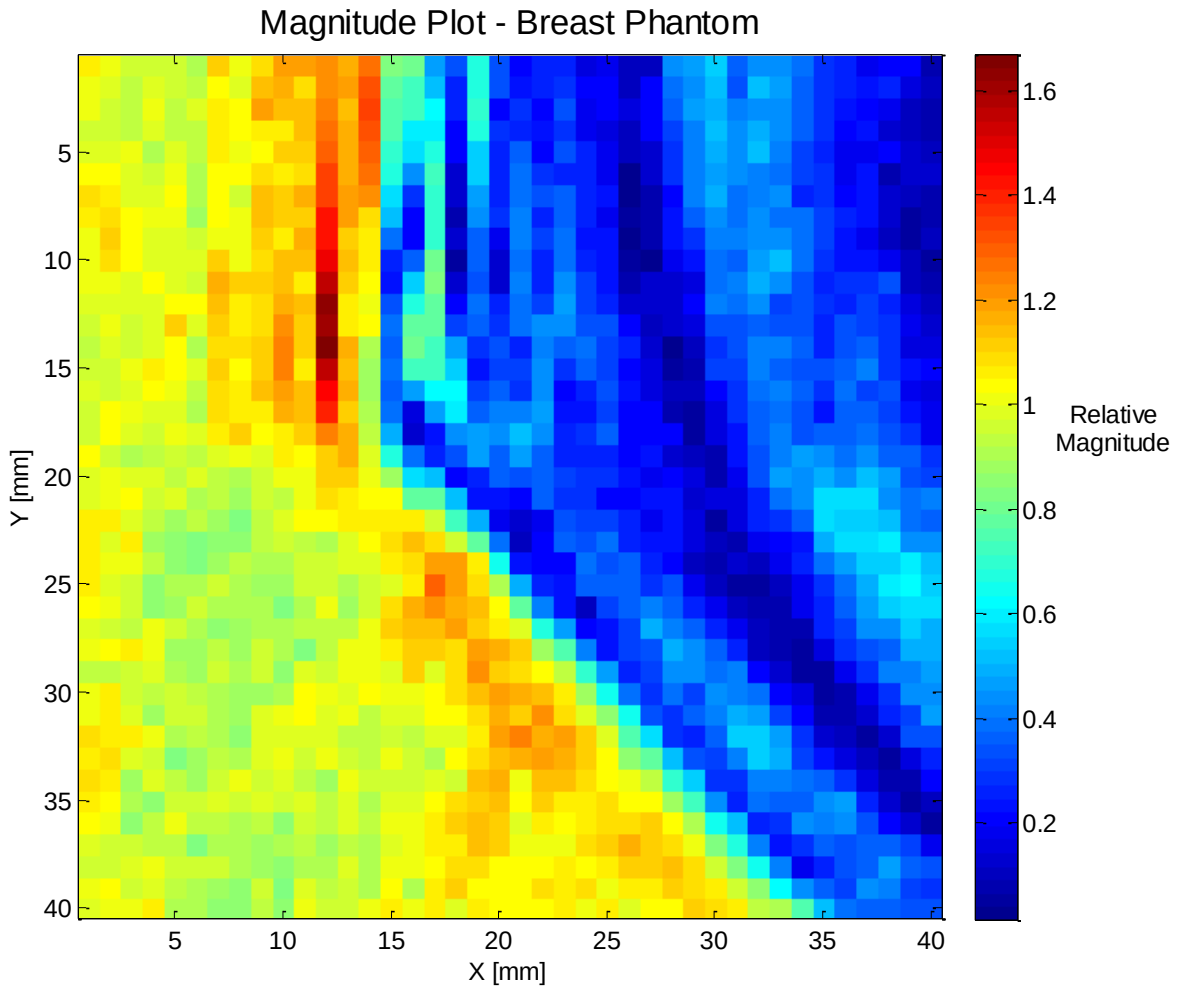

Figure 41: Two-dimensional magnitude projection of an ultrasound breast phantom.

Figure 42 shows the phase projection for the same scan. Absent are the refractive effects seen in the magnitude projection: signal amplitude is sufficient for phase determination even in areas of low signal magnitude. The absence of lens effects is due to the use of a spatial filter, which prevents waves that did not pass straight though the object (more or less) from creating an image. The beam is also able to undergo a phase change of 12.5 radians (roughly 4π) and still be readable. The maximum distance travelled through the phantom in this image is approximately 160 mm.

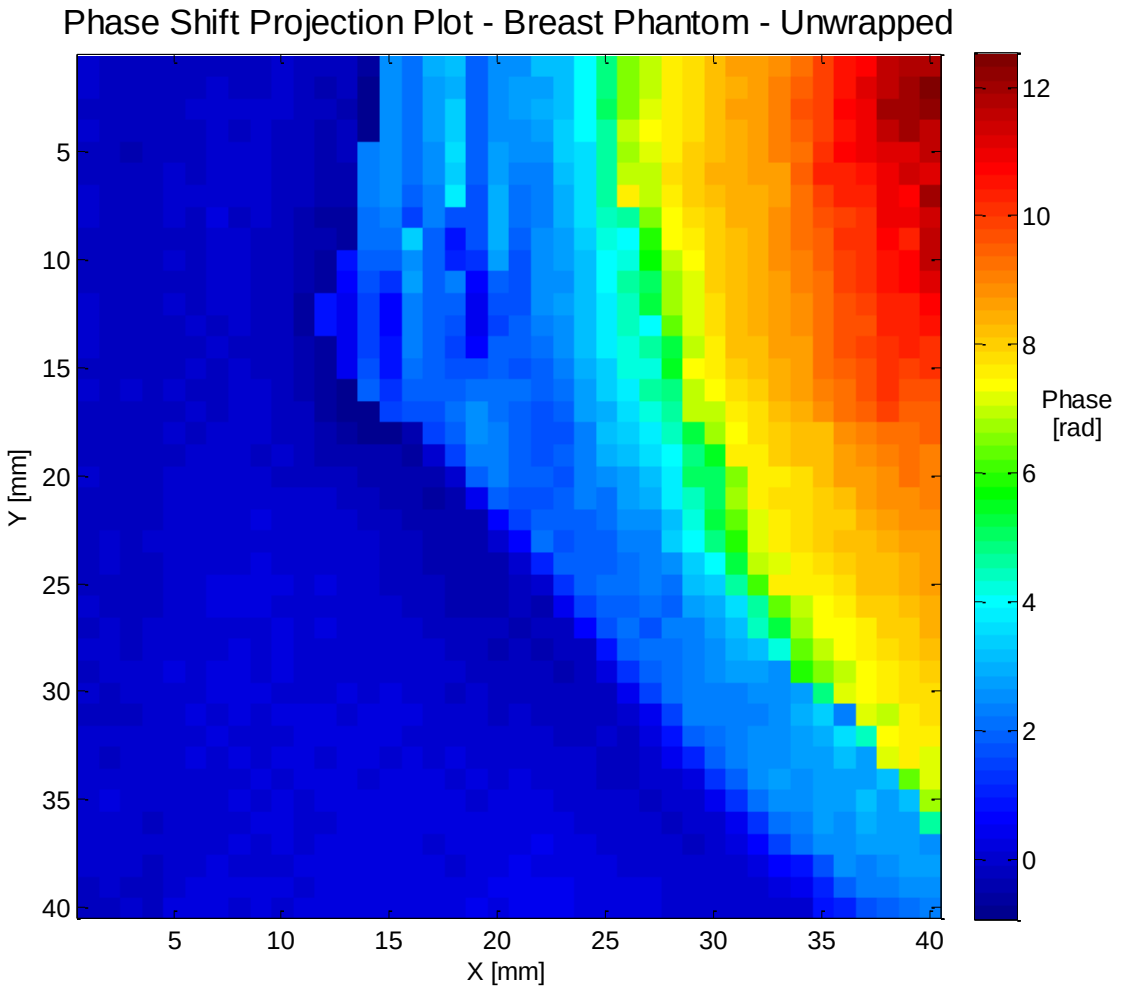

Figure 42: Two-dimensional phase projection of an ultrasound breast phantom.

It is difficult to make out any of the randomly placed lesions in this scan even though the lesions have a different speed of sound. Their presence is masked by the phase magnitude of the phantom. The phase of the wave represents a coupling of the distance and speed of sound through the object – this is why tomographic reconstruction, where spatial and speed components are separated out, is necessary.

Figure 43 shows the projection from Figure 42 overlaid on a profile view of the breast phantom. There is good spatial agreement between the two, showing that Figure 42 is a true projection of the phantom.

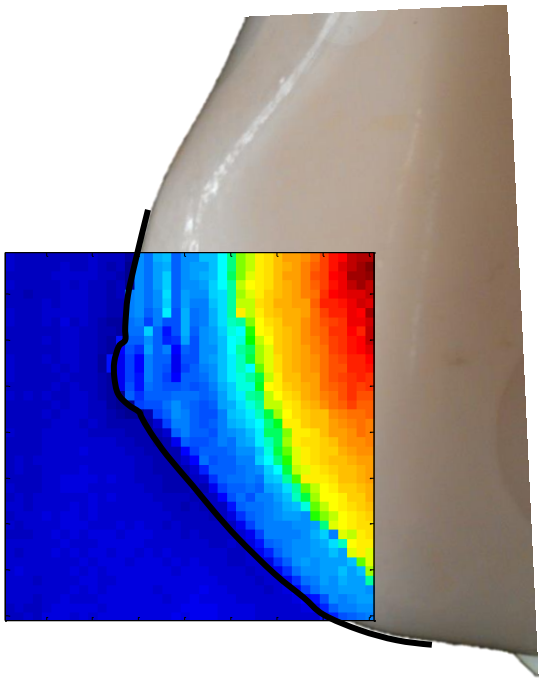

Figure 43: Phase projection overlaid on an image of the breast phantom.

5.3 SINOGRAMS

One dimensional projections are arranged into sinograms when imaging the object over multiple angles. This is done for both the magnitude and phase projections. Figure 44 shows five magnitude sinograms collected using the prostate phantom, and Figure 45 shows the phase sinograms from the same test. The phantom was imaged using a frequency of 1.412 MHz and 20 V_{pp}.

The sinograms are plotted showing the x position (in units of pixels) and the angular rotation of the specimen. The colours represent the peak-to-peak voltage generated at the receiver.

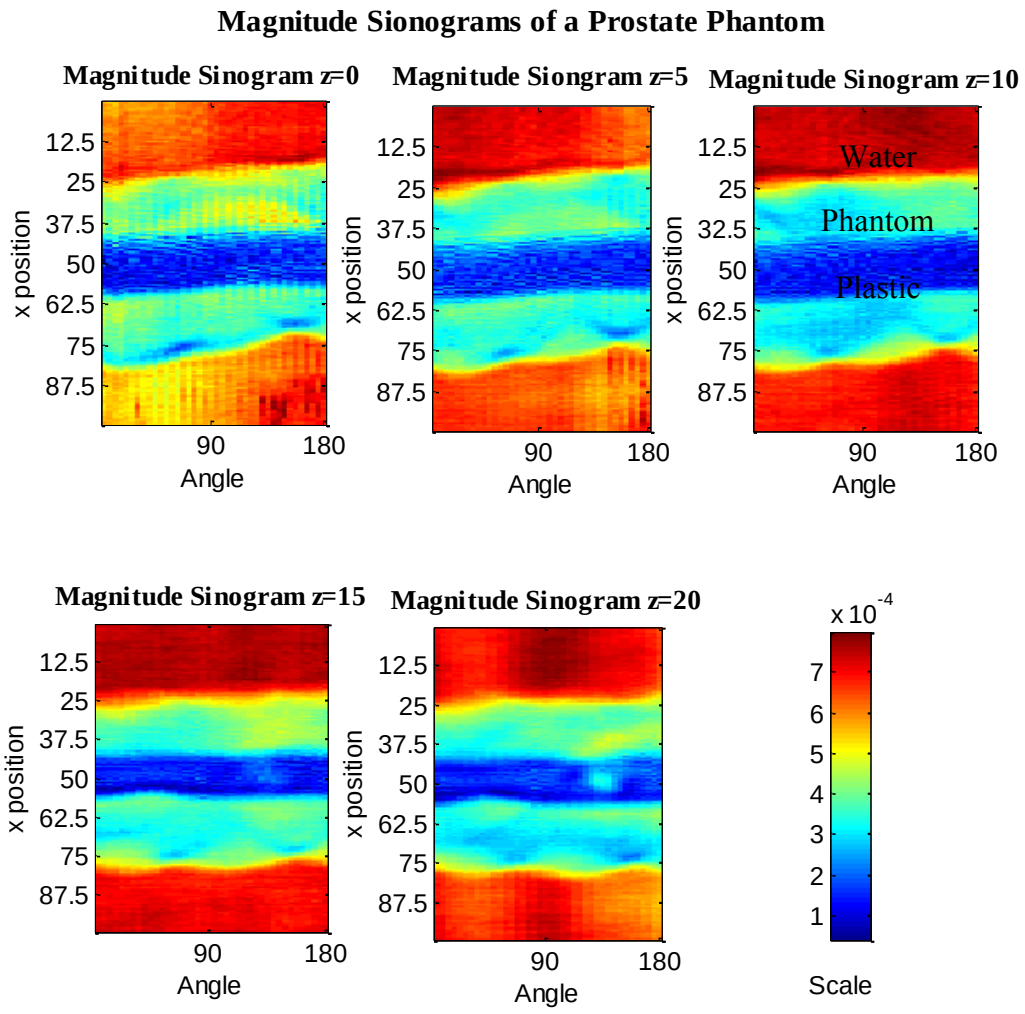

Figure 44: Magnitude sinograms of a prostate phantom in arbitrary z = 0 to z = 20 mm slices.

The sinograms show the presence of an object centered in the beam; however, not much information can be immediately garnered from the images. The highest intensity occurs when the beam passes only through water (seen as red). The beam is highly attenuated by the plastic core (seen as dark blue), and is attenuated to a lesser degree by the phantom itself (seen as light blue). A phase shift sinogram is recorded concurrently with the magnitude sinogram.

From Figure 45 we can see that there is a strong phase object in the center of each phase shift sinogram, causing a phase shift of approximately -9 (or roughly

two and a half waves advancement at 1.412 MHz). The surrounding water (seen as red) produces a phase shift of roughly -4. This will later be used as a reference when producing the speed of sound tomograms to turn the relative speed of sound into an absolute measurement.

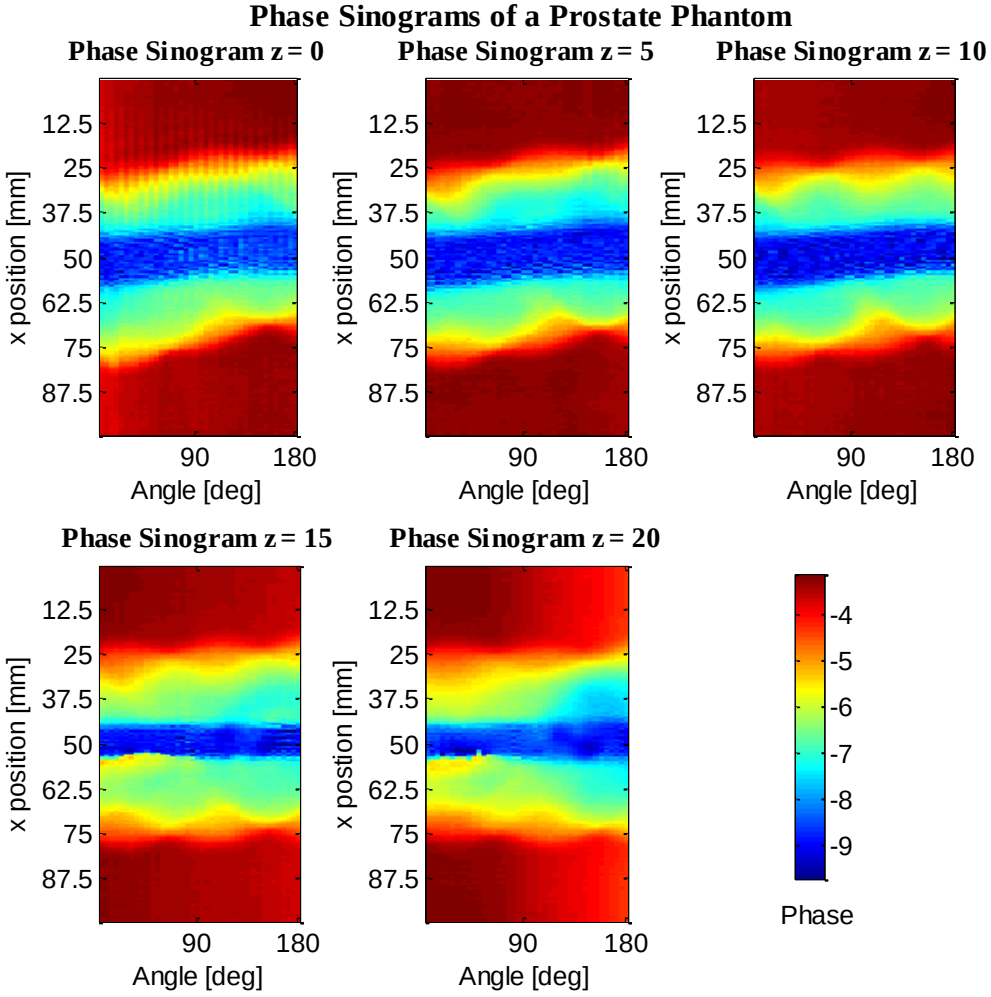

Figure 45: Phase sinograms of a prostate phantom in arbitrary z = 0 to z = 20 mm slices. A strong phase object can be seen centered in the image.

It is important to note that these sinograms have been unwrapped.

5.4 TOMOGRAMS

Some of the tomograms of the prostate phantom are presented below. Both speed of sound and attenuation coefficient tomograms are shown in Figure 46 and

Figure 47, respectively. A 1.508 MHz sine wave was used to drive the emitter at 20 V_{pp}. 41 projections were taken over 180 degrees with an even spacing between projections. 160 pixels were recorded over 100 mm for each projection, giving a pixel spacing of 625 μm. Planes commencing at an arbitrary z = 0 plane (roughly at the bottom of the prostate phantom) were imaged every 5 mm until 30 mm (7 planes in total). The prostate phantom was immersed in water at 22°C, which has a speed of sound of 1488 m/s.

5.4.1 Speed of Sound Tomograms

Figure 46 shows speed of sound tomograms of the prostate phantom taken at seven different z planes (normal to beam direction) within the object. Speed of sound tomograms are generated from phase sinograms (see section 5.3) using the process outlined in Section 3.4.3. It is not until reconstruction that the data collected using this imaging method can truly be analysed as speed of sound and distance information are separated out from the phase information.

We can see four distinct regions within each tomogram: the surrounding water (with a speed of sound of 1488 m/s at 22 °C – blue), the "healthy tissue" in the prostate phantom (~1522 m/s – light blue), two "diseased" regions (A and B: 1534 m/s – green), and the plastic core (1585 m/s – red). The diseased regions appear in multiple tomograms (at z = 10, 15, 20, and 25 mm) and in the same locations, indicating that these are spherical regions of a different speed of sound than the surrounds. The tomograms taken along the z = 0 and z = 5 mm planes suffer from artifacting (the lines emanating from the center of the image) which is a result of the neoprene cork used to support the phantom during imaging. Also visible is what appears to be a smearing of the center plastic region in the negative y-direction. This is a result of temperature increases during imaging. The increase in

temperature causes an increase in the speed of sound of the water, which in turn causes the waves to arrive earlier at the end of the scan, creating an offset in the sinogram.

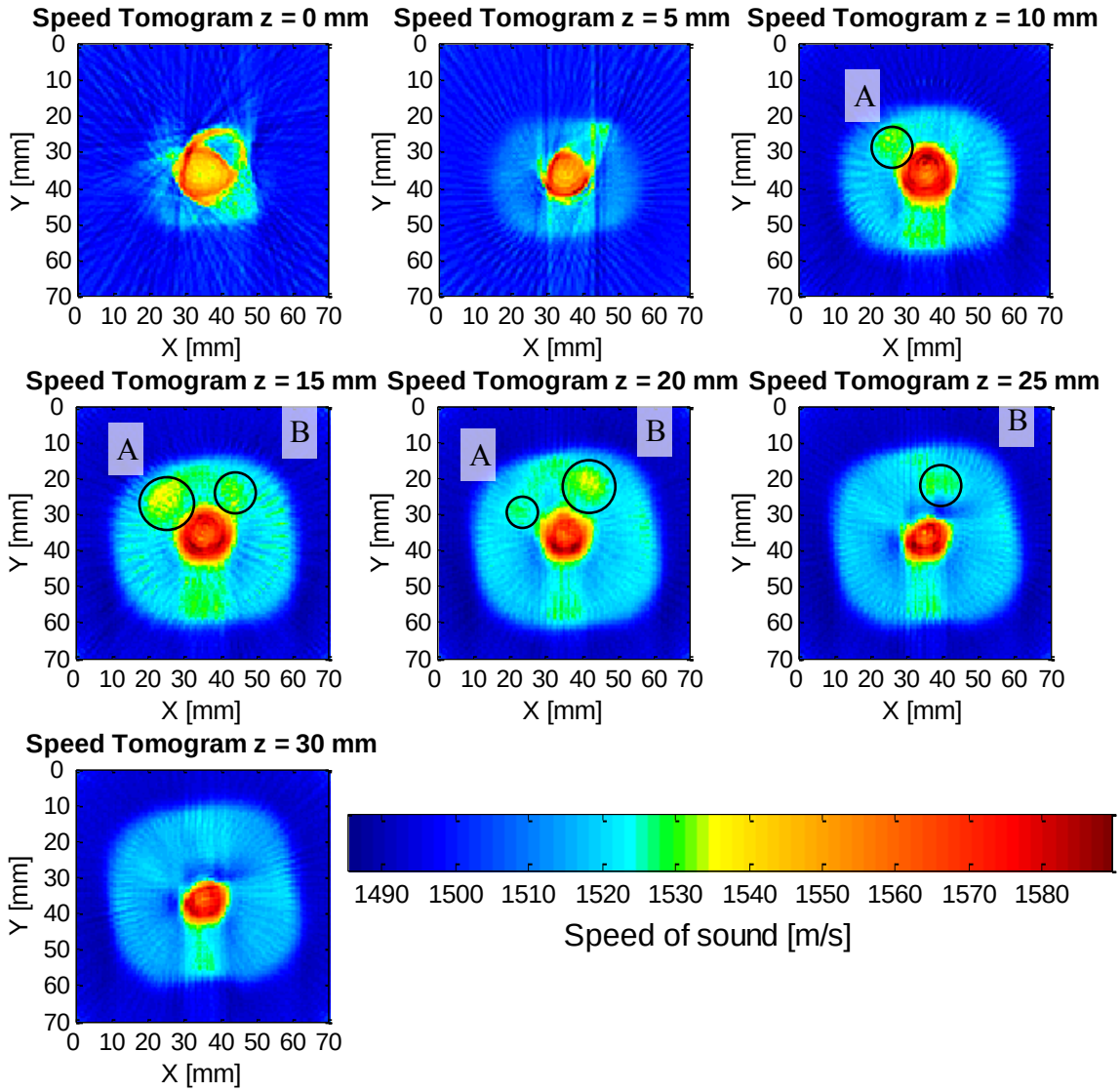

Figure 46: Speed of sound distribution in the prostate phantom at seven different planes. Regions 'A' and 'B' are the lesions inside the phantom.

5.4.2 Attenuation Coefficient Tomograms

Tomograms showing the localized attenuation coefficient of the prostate were produced concurrently with the speed of sound tomograms. One of the benefits of this imaging process is the production of two data sets showing different object

information. Figure 47 shows the attenuation tomograms taken of the prostate phantom.

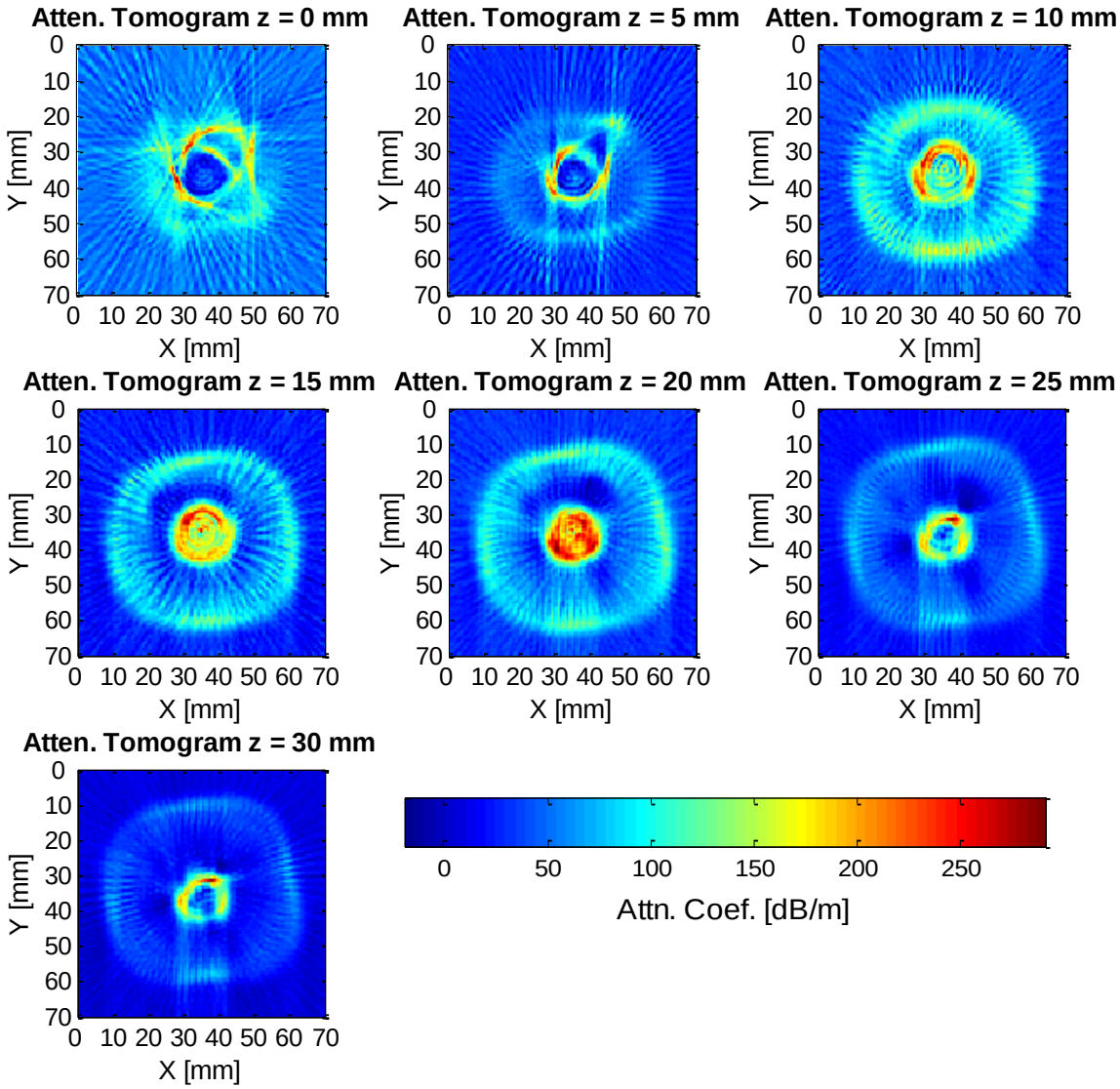

Figure 47: Attenuation coefficient distribution in the prostate phantom at seven different planes.

Similar to Figure 46, the z = 0 mm tomogram has artefacts caused by the use of the cork impregnated neoprene sheet used to hold the phantom – this material has a very high attenuation coefficient. Interfaces appear to have the highest attenuation coefficients – this can be attributed to reflection. Successive z planes appear to have lower attenuation coefficients. The most probable explanation for

this is that the phantom becomes more transparent as it slowly absorbs the surrounding water.

CHAPTER 6 – DISCUSSION AND CONCLUSIONS

6.1 DISCUSSION

An acoustic tomographic scanner capable of recording the change in phase and intensity of an acoustic wave that passed through a specimen was designed and constructed. This instrument was used to successfully record the information necessary to produce both speed of sound and acoustic attenuation tomograms, which can be recorded at the same time. ZEMAX optical design software was employed for the design of the instrument, and MATLAB was used to control imaging and analyse results. The instrument is capable of autonomously imaging a specimen transparent to sound. Two different designs were built – one which interrogates the object with a collimated acoustic beam, and one which uses a confocal beam. Results from the confocal tomographic scanner have been presented in this thesis, while further testing of the collimated scanner will continue with a linear piezoelectric array detector.

An aperture is used to spatially filter the projections captured by the scanner. This allows the scanner to capture projections free of any scattered or refracted waves. If recorded, these scattered waves would alter the phase and intensity of each projection, making the assumption that each projection is a "true" projection of the object invalid. This assumption is a necessary condition for the use of tomographic reconstruction algorithms.

A tomographic reconstruction algorithm best suited to the parameters used to image the prostate phantom was chosen based on a simulation. A least squares algorithm, with relaxation parameter λ=1, was chosen based on this simulation. It

was assumed that the noise recorded in the projections was Gaussian; however, further work should include an error analysis to determine the actual error distribution. The least squares algorithm performed well in terms of computation time and overall error. The ability to do a majority of the computational work prior to imaging, and the ability to re-use the least-squares matrix produced before experimentation on scans with the same geometry gives this method a speed advantage over other post-imaging type algorithms.

An improvement over the original holographic method for determining the phase shift in the interrogating acoustic beam caused by the specimen was made. This was done by determining the phase shift of the wave by comparing the phase of the driving and received signals. Doing this allowed the phase of the wave to be determined at a single point, negating the need to record a hologram of upwards of 64 pixels. This phase-shift method was used to determine the speed of sound in water at 21°C, producing results that differed by 2.8% from accepted values. Prior to this improvement a hologram of at least 64 points needed to be recorded to determine the phase shift of a pencil beam passing through the object. The ability to obtain this information at a single point increased accuracy by reducing spatial averaging and reduced imaging time.

The confocal scanner was used to take two-dimensional projections of a breast phantom. The shape of each projection matches the shape and size of the phantom. An increase in phase change can be seen with increasing thickness in the phase projection – as expected. Lens effects can be seen in the magnitude projection plot: this makes accurate tomographic reconstruction of this parameter difficult without the use of a bent-ray reconstruction algorithm. Lens effects are not seen in the phase plot – this would allow for accurate speed of sound reconstruction.

Tomograms of a prostate phantom were taken with the confocal apparatus. Both the acoustic attenuation coefficient and the speed of sound inside the phantom were plotted in seven different planes spaced at 5 mm. The phantom was clearly defined in both plots. The speed of sound tomograms show two spherical regions of a different speed of sound present in the phantom. These regions are of the correct nature and size to be the "diseased" lesions implanted by the manufacturer.

The ability to supply medical professionals with two potentially useful diagnostic data sets for the detection of breast cancer (both speed of sound and attenuation tomograms) is what makes this imaging method an excellent candidate for further research.

6.2 Future Work

6.2.1 Testing and Validation

A tomography phantom with a known speed of sound should be created and tested. This could be done by filling balloons with glycerine (1904 m/s) or ethyl alcohol (1144 m/s). A phantom to test the resolution of the instrument should be procured. An ideal phantom would contain cylinders of varying known diameters, with decreasing spacing between cylinders. The cylinders should have a different speed of sound and attenuation coefficient than the surrounding media to ensure they can be seen in both tomograms.

6.2.2 Physical Design and Ideas for a Clinical Device

The equipment used for these proof-of-concept devices requires some changes before a clinical trial-ready machine can be made. The linear actuators used to move the specimen do not have a long enough stroke. The motor controller can only drive 3 linear actuators, and each actuator has a stroke of 50 mm. This limits the total travel of the specimen to a combined 150 mm. The breast phantom

measures 230 mm through its thickest section, and has a height of 76 mm, requiring an x stroke of 300 mm and a y stroke of 100 mm, which would be similar to a clinical device. In the future, the specimen should remain stationary and the apparatus should translate / rotate. This lends itself better to use in a clinical setting.

The focused design is limited to a horizontal stroke of 175 mm, as the object will collide with the emitter and receiver. The collimated design does not have this limitation, as the emitter can be placed a distance away from the first mirror. It is therefore recommended that a clinical device use the collimated mirror set-up.

The time required to capture one tomogram varies with the number of angles and the number of pixels. Currently, one pixel is recorded at a time, and the time required for a tomogram measuring 113 x 113 pixels taken over 41 angles is roughly 75 minutes. The incorporation of a detector with multiple piezo transducers arranged in a linear array will decrease the imaging time significantly. A much improved version would use a two-dimensional array, allowing multiple sections to be imaged at once. It is then conceivable that one projection would take around 1 second, meaning a detailed tomogram of the entire specimen could be captured in less than two minutes.

In a clinical setting the patient would lie prone with one breast immersed in the imaging tank, as is done by others [3], [6]. Another possibility is the use of an impedance-matched liquid or gel held around the breast by a membrane, allowing for the process to be carried out in a sitting position.

6.2.3 Dispersion Tomography and Bent Ray Reconstruction Methods

Others have shown that different tissues disperse acoustic waves in differing amounts [15], [26], [27], [36], making this imaging modality a candidate for

detecting cancerous lesions in the breast and elsewhere. However, to the best knowledge of the author, no one has applied tomography to acoustic dispersion imaging. Without the use of tomography, a localised measure of the speed of sound difference between two frequencies in the specimen cannot be made, nor can the location of any dispersive tissues be discovered.

The acoustic tomographic scanners described in Section 3.2 above are also capable of acoustic dispersion tomography. Instead of driving the acoustic emitter with one frequency, two (or many) are used. The recorded signal is then Fourier transformed, and the phase of both frequencies is recorded. The phase information is then used to determine the relative time of flight of each frequency (compared to water). The time difference between the two frequencies is then calculated and plotted in a sinogram, which is then reconstructed to produce a tomogram showing the speed of sound difference between the two frequencies inside the object. The amplitude of each signal can also be recorded – this is potentially valuable information as cancerous lesions may absorb higher frequencies more readily than lower frequencies.

The use of a dispersion index could provide a third modality to this imaging method. There are no extra hardware requirements. Speed of sound, absorption coefficient, and dispersion tomograms can be recorded and created at once.

An experiment was devised to test acoustic dispersion tomography. Two function generators were used to create sine waves at 800 kHz and 1.5 MHz. A software filter was created to capture the relative phase and amplitude of the waves. Unfortunately, a hardware malfunction prevented any meaningful data from being recorded. Future improvements to the amplification circuit used to capture the receiver signal should rectify these problems.

Utilizing a reconstruction algorithm that accurately models the ray paths through the object would produce results with greater accuracy. The Fast Marching Method would be well suited to spatially-filtered continuous-wave acoustic tomography.

6.3 FINAL CONCLUSIONS

This work included the design and construction of a proof of concept prototype acoustic tomography scanner that could be modified for use in a clinical setting. The confocal acoustic tomographic scanner described herein was used to successfully image a prostate phantom. The surrounding water, prostate tissue, diseased lesions within the prostate, and the plastic core were clearly visible in the tomogram and the measured speed of sound values within the prostate phantom fell within the range provided by the manufacturer.

This imaging method uses a continuous ultrasonic wave to take speed of sound measurements inside a specimen and an aperture to block scattered rays that do not positively contribute to the measurement. The phase of the wave is used to determine the time-of-flight through the specimen, which differs from other devices that rely on an ultrasonic pulse. This work has laid the foundation for further investigation of spatially-filtered continuous-wave acoustic tomography as a quantitative diagnostic tool for the detection of breast cancer.

REFERENCES

[1] N. Duric, P. Littrup, L. Poulo, A. Babkin, R. Pevzner, E. Holsapple, O. Rama, and C. Glide, "Detection of breast cancer with ultrasound tomography: First results with the Computed Ultrasound Risk Evaluation (CURE) prototype," *Medical Physics*, vol. 34, no. 2, p. 773, 2007.

[2] P. L. Carson, C. R. Meyer, A. L. Scherzinger, and T. V. Oughton, "Breast Imaging in Coronal Planes with Pulse Echo and Transmission Ultrasound Simultaneous," vol. 214, no. 4525, pp. 1141–1143, 2012.

[3] N. V. Ruiter, M. Zapf, T. Hopp, R. Dapp, E. Kretzek, M. Birk, B. Kohout, and H. Gemmeke, "3D ultrasound computer tomography of the breast: A new era?," *European Journal of Radiology*, vol. 81, pp. S133–S134, Sep. 2012.

[4] C. D. Lehman, M. P. André, B. a Fecht, J. M. Johansen, R. L. Shelby, and J. O. Shelby, "Through-transmission US applied to breast imaging.," *Academic radiology*, vol. 7, no. 2, pp. 100–7, Feb. 2000.

[5] S. Li, M. Jackowski, D. P. Dione, T. Varslot, L. H. Staib, and K. Mueller, "Refraction corrected transmission ultrasound computed tomography for application in breast imaging," *Medical Physics*, vol. 37, no. 5, p. 2233, 2010.

[6] C. Li, N. Duric, P. Littrup, and L. Huang, "In vivo breast sound-speed imaging with ultrasound tomography.," *Ultrasound in medicine & biology*, vol. 35, no. 10, pp. 1615–28, Oct. 2009.

[7] M. O. et. al Leach, "Screening with magnetic resonance imaging and mammography of a UK population at high familial risk of breast cancer: a prospective multicentre cohort study (MARIBS).," *Lancet*, vol. 365, no. 9473, pp. 1769–78, 2005.

[8] E. Tohno, E. Ueno, and H. Watanabe, "Ultrasound screening of breast cancer.," *Breast cancer (Tokyo, Japan)*, vol. 16, no. 1, pp. 18–22, Jan. 2009.

[9] A. Tarantola, *Inverse Problem Theory and Methods for Model Parameter Estimation*. Philadelphia: Society for Industrial and Applied Mathematics, 2005.

[10] B. D. Sawicka, "Computed Laminography, Limited-View Tomography and Fully 3-D Image Reconstruction," in *Proceedings of the 1995 Symposium on Applied Mathematics, AECL Report RC-1458, CMS-95-03*, 1995, pp. 70–74.

[11] P. C. Hansen, "The discrete picard condition for discrete ill-posed problems," *BIT*, vol. 30, no. 4, pp. 658–672, Dec. 1990.

[12] M. Saxild-Hansen, "AIR Tools - A MATLAB Package for Algebraic Iterative Reconstruction Techniques," M.Sc. thesis, Dept. Informatics Math Modelling, Technical University of Denmark, Kongens Lyngby, Denmark, 2010.

[13] L. Landweber, "An iteration formula for Fredholm integral of the first kind," *American Journal of Mathematics*, vol. 73, pp. 615–624, 1951.

[14] Advisory Group on Non-ionising Radiation, "Health Effects of Exposure to Ultrasound and Infrasound," Health Protection Agency, London, UK, 2010.

[15] Y. Levy, Y. Agnon, and H. Azhari, "Ultrasonic speed of sound dispersion imaging.," *Ultrasound in medicine & biology*, vol. 33, no. 5, pp. 762–7, May 2007.

[16] S. Atalick, "Confocal Acoustic Holography for Non-Invasive 3D Temperature and Composition Measurement," M.A.Sc thesis, Dept. Mech. Eng., University of Victoria, Victoria, B.C., 2007.

[17] I. Jovanovic, "Inverse Problems in Acoustic Tomography: Theory and Applications," Ph.D. dissertation, School Comp. Comm. Sci., Ecole polytechnique fédérale de Lausanne, Lausanne, Switzerland, 2008.

[18] V. E. Ostashev, *Acoustics in moving inhomogeneous media*. London: Spon Press, 1997, p. 259.

[19] J. Ferlay, H.-R. Shin, F. Bray, D. Forman, C. Mathers, and D. M. Parkin, "Estimates of worldwide burden of cancer in 2008: GLOBOCAN 2008.," *International journal of cancer. Journal international du cancer*, vol. 127, no. 12, pp. 2893–917, Dec. 2010.

[20] C. E. Ingram and L. Wyld, "Imaging techniques in screening for breast cancer," *Surgery (Oxford)*, vol. 25, no. 6, pp. 257–260, Jun. 2007.

[21] P. C. Gøtzsche and M. Nielsen, "Screening for breast cancer with mammography," *Cochrane database of systematic reviews (Online)*, no. 1, p. CD001877, Jan. 2011.

[22] J. Greenleaf, "Quantitative cross-sectional imaging of ultrasound parameters," in *Ultrasonics Symposium Proceedings*, 1977, pp. 989–995.

[23] R. Jirik, I. Peterlik, N. Ruiter, J. Fousek, R. Dapp, M. Zapf, and J. Jan, "Sound-speed image reconstruction in sparse-aperture 3-D ultrasound transmission tomography," *IEEE Transactions on Ultrasonics, Ferroelectrics and Frequency Control*, vol. 59, no. 2, pp. 254–264, Feb. 2012.

[24] J. Brink and J. Carson, "Use of Tomography for Diagnostic Purposes in Primary Ciliary Dyskineasia," *Microscopy and Microanalysis*, vol. 16, no. S2, pp. 970–971, Aug. 2010.

[25] S. A. Johnson, D. T. Borup, J. W. Wiskin, F. Natterer, F. Wuebbling, Y. Zhang, and C. Olsen, "Apparatus and method for imaging with wavefields using inverse scattering techniques," U.S. Patent 6,005,9161999.

[26] F. Dunn, "Acoustic properties of selected bovine tissues in the frequency," vol. 98, no. 3, pp. 3035–3039, 1995.

[27] K. R. Marutyan, M. Yang, S. L. Baldwin, K. D. Wallace, M. R. Holland, and J. G. Miller, "The frequency dependence of ultrasonic velocity and the anisotropy of dispersion in both freshly excised and formalin-fixed myocardium.," *Ultrasound in medicine & biology*, vol. 32, no. 4, pp. 603–10, Apr. 2006.

[28] J. Sethian, "A fast marching level set method for monotonically advancing fronts.," *Proceedings of the National Academy of Sciences of the United States of America*, vol. 93, no. 4, pp. 1591–5, Feb. 1996.

[29] R. A. Herring, "Confocal scanning Laser holography, and an associated microscope : a proposal," *Optik*, vol. 105, no. 2, pp. 65–68, 1996.

[30] P. Jacquemin, "A Confocal Scanning Laser Holography Microscope to Non-Intrusively Measure the Three-Dimensional Temperature and Composition of a Fluid (Proposed)," Ph.D. dissertation, Dept. Mech. Eng, University of Victoria, Victoria, B.C., 2009.

[31] S. Lai, R. a McLeod, P. Jacquemin, S. Atalick, and R. Herring, "An algorithm for 3-D refractive index measurement in holographic confocal microscopy.," *Ultramicroscopy*, vol. 107, no. 2–3, pp. 196–201, 2007.

[32] R. A. Herring, P. Jacquemin, B. D. Sawicka, and S. Atalick, "Developing a confocal acoustic holography microscope for non-invasive 3D temperature and composition measurements.," *Ultramicroscopy*, vol. 109, no. 7, pp. 830–6, Jun. 2009.

[33] S. W. Smith, *The Scientist and Engineer's Guide to Digital Signal Processing*, vol. 3, no. 3. California Technical Publishing, 1997, p. 626.

[34] L. Aiello, D. Riccio, P. Ferraro, S. Grilli, L. Sansone, G. Coppola, S. De Nicola, and a. Finizio, "Green's formulation for robust phase unwrapping in digital holography," *Optics and Lasers in Engineering*, vol. 45, no. 6, pp. 750–755, Jun. 2007.

[35] R. Lanari, "Interferometric SAR Phase Unwrapping Using Green's Formulation," vol. 34, no. 3, 1996.

[36] Y. Sugawara, O. B. Wright, and O. Matsuda, "Direct access to the dispersion relations of multiple anisotropic surface acoustic modes by Fourier image analysis," *Applied Physics Letters*, vol. 83, no. 7, p. 1340, 2003.